Cell Stem Cell

Short article

Patient iPSC models reveal glia-intrinsic phenotypes in multiple sclerosis

Graphical abstract

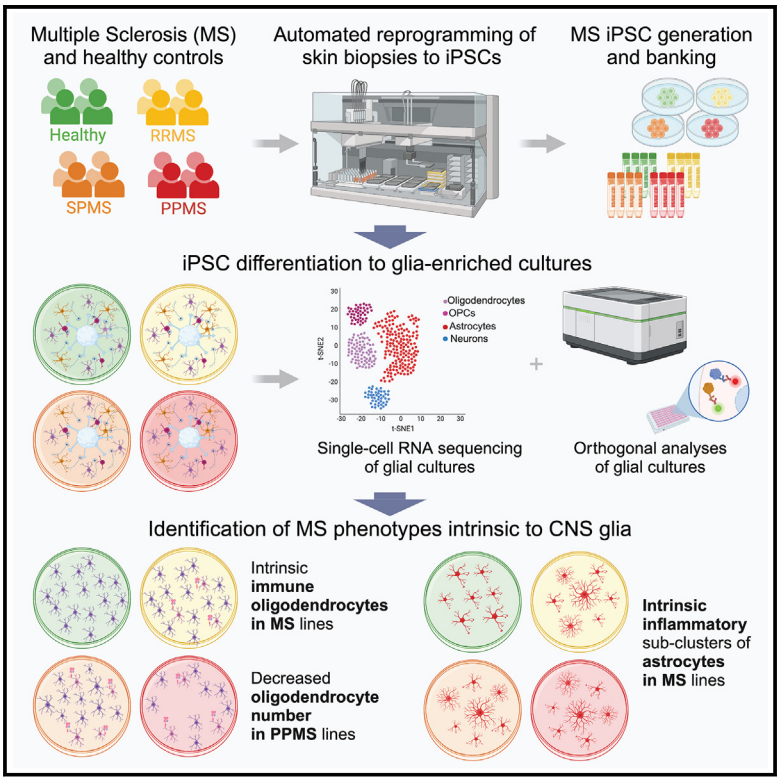

Highlights

- Glia-intrinsic MS phenotypes in iPSC-derived cells not exposed to inflammation
- Decreased number of iPSC-derived primary progressive MS oligodendrocytes
- Immune and inflammatory profiles in iPSC-derived MS oligodendrocytes and astrocytes
- iPSC-derived MS astrocytes transcriptionally mirror reactive astrocytes from MS brains

Authors

Benjamin L.L. Clayton, Lilianne Barbar, Maria Sapar, ..., Patrizia Casaccia, Paul J. Tesar, Valentina Fossati

Correspondence

paul.tesar@case.edu (P.J.T.), vfossati@nyscf.org (V.F.)

In brief

Clayton, Barbar, and colleagues compared iPSC lines from people with relapsing remitting multiple sclerosis (MS), primary progressive MS, and secondary progressive MS and healthy individuals. Differentiation into glial cells and their single-cell transcriptomic profiling revealed MS-intrinsic immune and inflammatory phenotypes in oligodendrocytes and astrocytes in the absence of inflammation or immune cells.

Clayton et al., 2024, Cell Stem Cell *31*, 1–13
October 3, 2024
https://doi.org/10.1016/j.stem.2024.08.002

CellPress

Please cite this article in press as: Clayton et al., Patient iPSC models reveal glia-intrinsic phenotypes in multiple sclerosis, Cell Stem Cell (2024), https://doi.org/10.1016/j.stem.2024.08.002

Cell Stem Cell

CellPress

Short article

Patient iPSC models reveal glia-intrinsic phenotypes in multiple sclerosis

Benjamin L.L. Clayton,[1,6] Lilianne Barbar,[2,5,6] Maria Sapar,[2] Kriti Kalpana,[2] Chandrika Rao,[2] Bianca Migliori,[2] Tomasz Rusielewicz,[2] The NYSCF Global Stem Cell Array® Team,[2] Daniel Paull,[2] Katie Brenner,[2] Dorota Moroziewicz,[2] Ilana Katz Sand,[3] Patrizia Casaccia,[4] Paul J. Tesar,[1,*] and Valentina Fossati[2,7,*]

[1]Institute for Glial Sciences, Department of Genetics and Genome Sciences, Case Western Reserve University School of Medicine, Cleveland, OH 44106, USA

[2]The New York Stem Cell Foundation Research Institute, New York, NY 10019, USA

[3]Corinne Goldsmith Dickinson Center for Multiple Sclerosis, Department of Neurology, Icahn School of Medicine at Mount Sinai, New York, NY 10129, USA

[4]Neuroscience Initiative, Advanced Science Research Center at CUNY, New York, NY 10031, USA

[5]Present address: Department of Developmental Biology, Washington University School of Medicine, St. Louis, MO 63110, USA

[6]These authors contributed equally

[7]Lead contact

*Correspondence: paul.tesar@case.edu (P.J.T.), vfossati@nyscf.org (V.F.)

https://doi.org/10.1016/j.stem.2024.08.002

SUMMARY

Multiple sclerosis (MS) is an inflammatory and neurodegenerative disease of the central nervous system (CNS), resulting in neurological disability that worsens over time. While progress has been made in defining the immune system's role in MS pathophysiology, the contribution of intrinsic CNS cell dysfunction remains unclear. Here, we generated a collection of induced pluripotent stem cell (iPSC) lines from people with MS spanning diverse clinical subtypes and differentiated them into glia-enriched cultures. Using single-cell transcriptomic profiling and orthogonal analyses, we observed several distinguishing characteristics of MS cultures pointing to glia-intrinsic disease mechanisms. We found that primary progressive MS-derived cultures contained fewer oligodendrocytes. Moreover, MS-derived oligodendrocyte lineage cells and astrocytes showed increased expression of immune and inflammatory genes, matching those of glia from MS postmortem brains. Thus, iPSC-derived MS models provide a unique platform for dissecting glial contributions to disease phenotypes independent of the peripheral immune system and identify potential glia-specific targets for therapeutic intervention.

INTRODUCTION

Multiple sclerosis (MS) is a chronic inflammatory and neurodegenerative disease of the central nervous system (CNS),[1] arising from a complex interplay between environmental factors, such as Epstein-Barr virus (EBV) infection,[2] and genetic predisposition.[3,4] During the early phase of the disease, MS most commonly manifests with focal neurological symptoms caused by acute demyelinating lesions with some degree of endogenous repair (relapsing remitting MS [RRMS][5]). Fewer individuals (<15%) experience a progressive course from disease onset that is associated with a worse prognosis (primary progressive MS [PPMS]).[6] Over time, most RRMS individuals develop secondary progressive MS (SPMS), characterized by steady accumulation of neurological disability related to failed repair mechanisms and neurodegeneration.[7] In RRMS, peripheral immune cell infiltration and inflammation are prominent, and therapies targeting B or T cells dramatically reduce new lesions and relapses.[8,9] Unfortunately, these therapies are modestly effective at preventing the neurodegeneration driving disease progression,[10] suggesting disease mechanisms that are independent of peripheral immunity. The mechanisms behind chronic MS progression are only partially understood, highlighting an urgent unmet need.

Accumulating single-cell transcriptome profiles of postmortem brains have shed light on glial-specific changes in MS,[11–13] involving astrocytes and oligodendrocytes. Genome-wide association studies (GWASs) and epigenomic studies have also highlighted glial aberrations in MS independent of peripheral immunity.[14,15] Studies of postmortem brains, however, cannot discern the intrinsic phenotypes of glial cells in MS from the effects of inflammation and immune cells. Human models based on induced pluripotent stem cell (iPSC) technology are increasingly used to investigate complex CNS disorders[16,17] and provide the opportunity to investigate glial dysfunction in MS.

Here, we combined iPSC disease modeling and single-cell transcriptomics to identify glial cell-intrinsic MS phenotypes

Please cite this article in press as: Clayton et al., Patient iPSC models reveal glia-intrinsic phenotypes in multiple sclerosis, Cell Stem Cell (2024), https://doi.org/10.1016/j.stem.2024.08.002

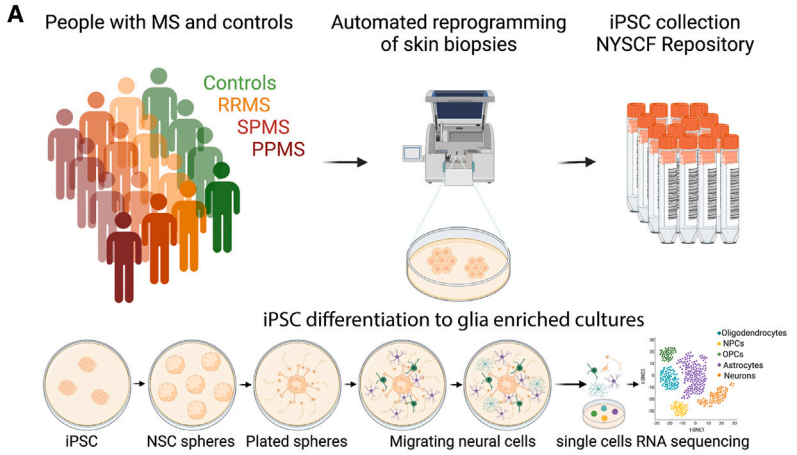

B

Group	Sample ID	Sex	Age at Collection
Healthy Control	HC01	F	65
Healthy Control	HC02	F	52
Healthy Control	HC03	M	51
Healthy Control	HC04	F	56
Relapsing-Remitting	RR01	F	56
Relapsing-Remitting	RR02	F	26
Relapsing-Remitting	RR03	F	30
Relapsing-Remitting	RR04	M	33
Secondary Progressive	SP01	F	63
Secondary Progressive	SP02	F	61
Secondary Progressive	SP03	F	46
Secondary Progressive	SP04	F	56
Primary Progressive	PP01	F	61
Primary Progressive	PP02	F	43
Primary Progressive	PP03	F	60
Primary Progressive	PP04	M	46

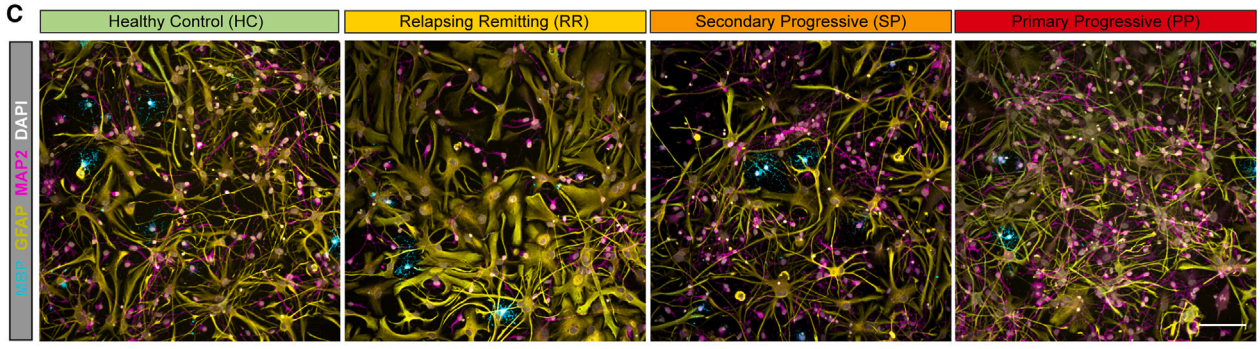

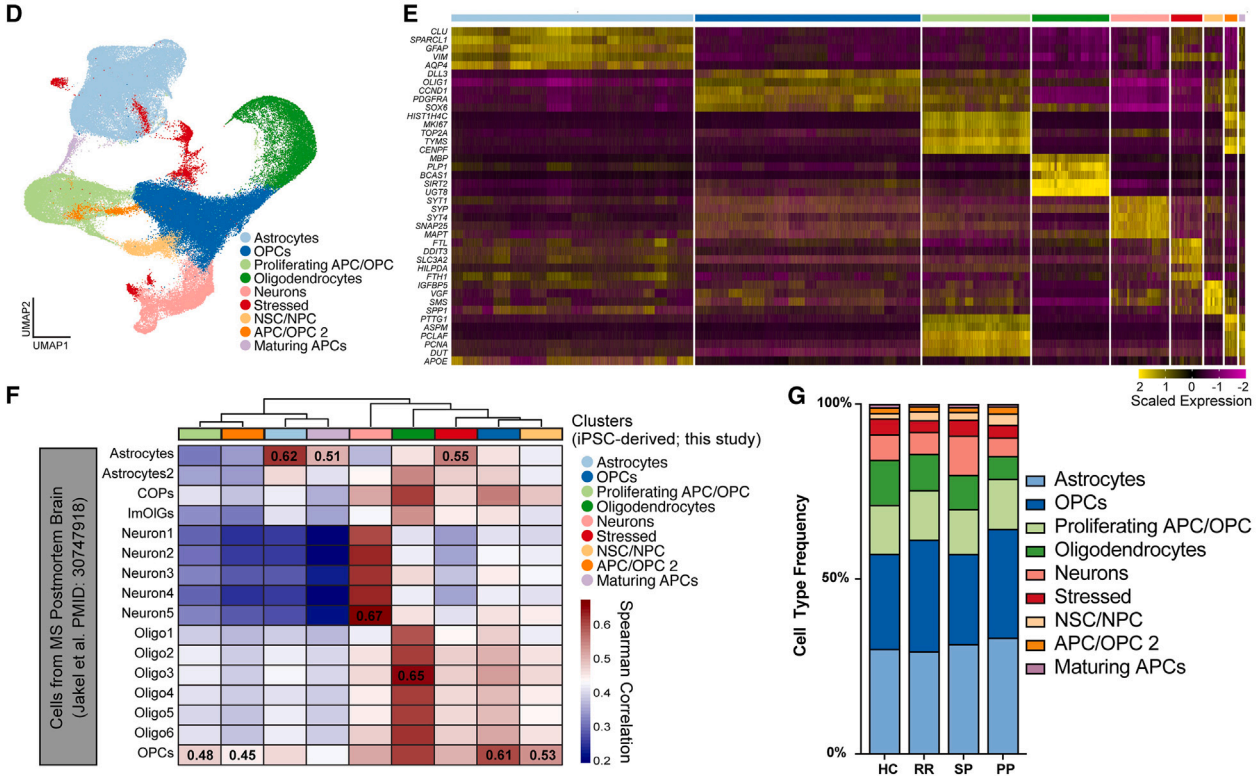

Figure 1. An iPSC-derived model to study CNS cell-intrinsic dysfunction in MS

(A) Schematic representation of iPSC reprogramming from people with MS and HC skin biopsies and differentiation of iPSCs into glial CNS cultures.

(B) Select demographic information for the 16 iPSC lines used for scRNA-seq analysis.

(legend continued on next page)

Please cite this article in press as: Clayton et al., Patient iPSC models reveal glia-intrinsic phenotypes in multiple sclerosis, Cell Stem Cell (2024), https://doi.org/10.1016/j.stem.2024.08.002

that occur in the absence of inflammatory stimuli or interactions with peripheral immune cells. We found that iPSC-derived cultures from people with PPMS generated fewer oligodendrocytes. Moreover, iPSC-oligodendrocyte lineage cells and iPSC-astrocytes from people with MS showed increased expression of immune and inflammatory genes that match those in MS postmortem brains. This study highlights the value of iPSC modeling for generating disease-relevant cell types and capturing glial cell-intrinsic phenotypes in MS.

RESULTS

Generation of an iPSC collection for MS research

For this study, we used 17 MS iPSC lines (6 RRMS, 6 SPMS, and 5 PPMS)[18] and 5 iPSC lines from healthy controls (HCs; Figures 1A, 1B, and S1A, Table 1). All iPSC lines were generated using the NYSCF Global Stem Cell Array®, a fully automated reprogramming process that minimizes line-to-line variability.[19] To characterize glial cells, we leveraged our previously published protocol[20,21] and differentiated iPSCs into cultures enriched in astrocytes and oligodendrocyte lineage cells (encompassing all stages from oligodendrocyte progenitor cells [OPCs] to mature oligodendrocytes) (Figures 1C, S1B, and S1C).

Single-cell transcriptional profiling of iPSC-derived neural cells from people with MS

Using 16 iPSC lines (4 HC, 4 RRMS, 4 PPMS, and 4 SPMS; Figure 1B, Table 2), we performed single-cell RNA sequencing on glia-enriched cultures, and we characterized a total of 122,228 cells with an average of 7,639 ± 1,141 cells per line (Figure S1D). Data were first filtered to remove doublets and low-quality cells and genes (details in STAR Methods and Figures S1E and S1F). Unsupervised clustering of the remaining cells identified 9 clusters shared by all individual samples (Figures 1D and S1G). We next used cluster-specific differentially expressed genes to assign a cell type to each cluster (Table S1). The largest identified cell clusters were: astrocytes (*GFAP* and *AQP4*), OPCs (*OLIG1* and *PDGFRA*), proliferating progenitor cells (*MKI67* and *TOP2A*), oligodendrocytes (myelin basic protein [*MBP*] and *PLP1*), neurons (*STMN2* and SCG2), and stressed cells with high expression of genes involved in stress response and apoptosis (*DDIT3, ATF5, BNIP3*; Figures 1E and S1G). Our data were consistent with previously reported classifications of cell-specific clusters from human MS brain tissues[11,12] (Figures 1F and S1H). Moreover, some of the GWAS-identified MS risk genes[22] were differentially expressed in MS compared with HC cells (Figure S1I). Thus, iPSCs from MS and HCs successfully differentiate into MS-relevant cell types and can be used for exploring glial-specific molecular and functional differences in MS.

iPSC-derived glial-enriched cultures from people with PPMS contain fewer oligodendrocytes

We next asked whether the frequency of cell types changed in iPSC-derived CNS cultures from MS compared with HC. Surprisingly, we found a consistent impairment in the generation of oligodendrocytes in PPMS cultures (6.45%, 2,061/31,909) compared with HC cultures (12.86%, 4,290/33,344; Figures 1G and S1J). To rule out a general defect in the differentiation potential of the MS lines, we assessed the generation of astrocytes and neurons and found no differences in the number of $CD49f^+$ astrocytes[23] (Figure S1K) or $MAP2^+$ neurons (Figures S1L and S1M) between MS and HC. Notably, we used a distinct protocol to differentiate iPSCs into cortical neurons,[24] since our oligodendrocyte protocol primarily yields glial cells and only results in a small number of immature neurons.

To further explore the potential decreased oligodendrocyte formation in PPMS cultures, we reclustered only the iPSC-derived oligodendrocyte lineage cells and identified five populations representing different stages of OPC differentiation into oligodendrocytes (Figure 2A; Table S1): three OPC clusters (34.31% OPCs.1, 27.19% OPCs.2, and 14.73% OPCs.3) expressing OPC markers, one cluster of newly formed oligodendrocytes (14.73%) expressing genes increased early in oligodendrocyte formation, and one cluster of mature oligodendrocytes (9.77%) expressing myelin genes (Figures 2A–2D and S2A). While all subtypes were present in all samples, the distribution of cell subtypes for each sample confirmed the decreased number of newly formed and mature oligodendrocytes, with a corresponding increase in OPCs only in PPMS cultures compared with HC, with no difference between MS types (Figures 2E and 2F).

Next, we performed orthogonal validation of oligodendrocyte formation via immunocytochemistry for OLIG2 and SOX10 (expressed at all stages in the oligodendrocyte lineage), O4, a marker of late adult progenitors and newly formed oligodendrocytes, and MBP, a major myelin component marking mature oligodendrocytes. No discernible differences were observed between MS and HC cultures regarding the proportion of total $OLIG2^+$ cells (Figure S2C). However, in agreement with our single-cell RNA sequencing (scRNA-seq) data, PPMS cultures exhibited a significant reduction in $O4^+$ or MBP^+ cells (Figures 2G–2I). To further investigate the timing of the impairment in differentiation, we quantified $SOX10^+$ and MBP^+ cells at three consecutive time points: days 55, 65, and 75. This longitudinal analysis showed that even in the early stages of differentiation, the overall number of $SOX10^+$ oligodendrocyte lineage cells remained comparable in PPMS and HC cultures. By contrast, although the number of MBP^+ oligodendrocytes increased over time, it consistently remained lower in PPMS cultures (Figure S2D). This deficit cannot be

(C) Representative images of iPSC-derived CNS cultures from HC, RRMS, SPMS, and PPMS. Cultures are stained for the mature oligodendrocyte marker MBP (teal), astrocyte marker GFAP (yellow), and neuron marker MAP2 (pink). Nuclei in gray (DAPI). Scale bars, 100 μm.
(D) Uniform manifold approximation and projection (UMAP) of integrated single-cell analysis from 4 HC, 4 RRMS, 4 SPMS, and 4 PPMS lines, showing major cell type clusters.
(E) Heatmap of the top 4 enriched genes for each cluster in (D).
(F) Heatmap depicting the correlation between clusters in (D) and cell types from scRNA-seq analysis of MS brain tissue (PMID: 30747918). Spearman correlation values generated using the R package ClustifyR.
(G) Distribution of cell types within iPSC-derived CNS cultures from HC, RRMS, SPMS, and PPMS.

Please cite this article in press as: Clayton et al., Patient iPSC models reveal glia-intrinsic phenotypes in multiple sclerosis, Cell Stem Cell (2024), https://doi.org/10.1016/j.stem.2024.08.002

Table 1. List of iPSC lines used in this study

Code	Repository Line name	Age at time of biopsy	Sex	Ethnicity	Disease state
HC01	050659-01-MR	65	F	Ashkenazi	Healthy control
HC02	051121-01-MR	52	F	Caucasian	Healthy control
HC03	050743-01-MR	51	M	Caucasian	Healthy control
HC04	051104-01-MR	56	F	Caucasian	Healthy control
HC05	051106-01-MR	57	F	Caucasian	Healthy control
RR01	AK0007-01-MR	56	F	African-American	Relapsing remitting MS
RR02	AK0028-01-MR	26	F	Caucasian	Relapsing remitting MS
RR03	AK0024-01-MR	30	F	African-American	Relapsing remitting MS
RR04	AK0014-01-MR	33	M	Caucasian	Relapsing remitting MS
RR05	AK0013-01-MR	54	M	Caucasian	Relapsing remitting MS
RR06	AK0027-01-MR	69	F	Caucasian	Relapsing remitting MS
SP01	AK0015-01-MR	63	F	Caucasian	Secondary progressive MS
SP02	AK0026-01-MR	61	F	Caucasian	Secondary progressive MS
SP03	AK0008-01-MR	46	F	Caucasian	Secondary progressive MS
SP04	AK0011-01-MR	56	F	Caucasian	Secondary progressive MS
SP05	AK0005-01-MR	65	F	Caucasian	Secondary progressive MS
SP06	AK0012-01-MR	51	F	African-American	Secondary progressive MS
PP01	AK0001-01-MR	61	F	Caucasian	Primary progressive MS
PP02	AK0009-01-MR	43	F	Caucasian	Primary progressive MS
PP03	AK0004-01-MR	60	F	Caucasian	Primary progressive MS
PP04	AK0010-01-MR	46	M	Caucasian	Primary progressive MS
PP05	AK0003-01-MR	52	F	Caucasian	Primary progressive MS

ascribed to differences in culture densities, as the total cell count (DAPI) showed no significant variance and did not correlate with the number of MBP^+ oligodendrocytes ($r = 0.2719$, Figure S2D).

We then performed pseudotime analysis to place oligodendrocyte lineage cells along the differentiation trajectory from OPCs to mature oligodendrocytes (Figure 2J). Density analysis confirmed once more that PPMS cultures contained fewer oligodendrocytes but more OPCs (Figures 2K and S2E). Moreover, we could not detect differences in the expression of oligodendrocyte differentiation gene modules with distinct expression patterns along the differentiation trajectory of OPCs to oligodendrocytes from HC cultures (Figure 2L; Table S2), despite PPMS cells showing a delay in the progression toward mature oligodendrocytes (Figure 2M). In addition, we did not find consistent differences in the expression of early oligodendrocyte markers (*BCAS1*,[25] *MYRF*,[26] and *TCF7L2*[27]) that would explain the decreased formation of mature oligodendrocytes in PPMS cultures (Figure S2B). To assess whether the reduced number of oligodendrocytes in PPMS cultures could result from increased cell death, we examined gene modules specific to known death mechanisms (i.e., apoptosis, ferroptosis, necroptosis, and pyroptosis) and found that ferroptosis genes were more highly expressed across all oligodendrocyte lineage cells in the PPMS cultures (Figure S2F). To rule out the possibility that vulnerable oligodendrocytes fell within the *stressed cells* cluster becoming excluded from the previous analyses, we compared the percentage of stressed cells in the MS and HC cultures and found no differences (Figure S2G); furthermore, upon examining the expression of the top 100 cell type-specific markers in cells from the *stressed* cluster, we found astrocytes (rather than OPC/oligodendrocytes) were the most affected population (Figure S2H). Even though the number of oligodendrocytes is decreased in PPMS cultures, the size of arborized oligodendrocytes was not reduced (Figures S2I and S2J). Together, these data suggest that increased ferroptosis in PPMS iPSC lines may lead to decreased mature oligodendrocytes in PPMS cultures, while morphology and oligodendrocyte gene expression programs are not altered.

iPSC-oligodendrocytes respond to myelinating drugs independent of disease state

Promoting mature oligodendrocyte formation and remyelination are major clinical goals in MS,[28] and multiple compounds that stimulate oligodendrocyte formation have been identified.[29–32] Nevertheless, it is not known whether MS-derived OPCs are responsive to oligodendrocyte-enhancing therapies or whether OPCs from distinct MS types respond differently to such drugs. To test this, we treated iPSC-derived cultures from HC and MS individuals with ketoconazole and TASIN-1, two small molecules that we have previously identified to promote oligodendrocyte formation by inhibiting enzymes in the cholesterol biosynthesis pathway.[33] Both treatments increased MBP^+ oligodendrocytes in all MS cultures (Figures 2N–2P and S2K), indicating that MS cells respond to potential remyelinating therapies regardless of MS type.

iPSC-derived MS oligodendrocytes exhibit an immune-like transcriptomic profile

Oligodendrocyte lineage cells undergo immunological changes in mouse models of MS and in human MS tissue that may

Please cite this article in press as: Clayton et al., Patient iPSC models reveal glia-intrinsic phenotypes in multiple sclerosis, Cell Stem Cell (2024), https://doi.org/10.1016/j.stem.2024.08.002

Table 2. iPSC lines used for each experiment

Line	HC01	HC02	HC03	HC04	HC05	RR01	RR02	RR03	RR04	RR05	RR06	SP01	SP02	SP03	SP04	SP05	SP06	PP01	PP02	PP03	PP04	PP05
scRNAseq	X	X	X	X		X	X	X	X			X	X	X	X			X	X	X	X	
RNAscope	X	X	X	X	X	X	X	X	X			X	X	X	X			X	X	X	X	X
KETO	X		X	X		X	X	X	X	X		X	X	X	X	X	X			X	X	X
TASIN	X	X	X	X	X								X	X	X			X			X	
iPSC-cortical neurons	X	X	X	X	X	X	X	X	X	X	X	X	X	X	X	X	X	X	X	X	X	X
IF for GFAP MAP2 MBP	X	X	X	X	X	X	X	X	X			X	X	X	X			X	X	X	X	X
OL morphology	X	X	X	X	X	X	X	X	X			X	X	X	X			X	X	X	X	X
IF staining for OL quantification	X	X	X	X	X	X	X	X	X			X	X	X	X			X	X	X	X	X
Astrocytes morphology	X	X	X	X	X	X	X	X	X			X	X	X	X			X	X	X	X	
HLA-ABC	X	X		X	X	X	X	X	X			X	X	X	X					X	X	

contribute to cell cytotoxicity, decreased oligodendrocyte formation, and ultimately failed remyelination.[11,34,35] Even in the absence of inflammatory stimuli or activation by peripheral immune cells, we found that iPSC-derived oligodendrocyte lineage cells from all MS groups expressed increased levels of major histocompatibility complex (MHC) class I transcripts HLA-A, HLA-B, and HLA-C (Figures 2Q and S2L). We performed live staining for HLA-ABC antigens and confirmed, at the protein level, the observations made from gene expression analysis (Figures 2R, 2S, and S2L). Thus, some immunological alterations may be intrinsic in MS-derived oligodendrocyte lineage cells and are likely amplified by chronic exposure to immune cells throughout the course of the disease.

iPSC-derived MS astrocytes exhibit an immune and inflammatory profile

Mounting evidence shows that reactive astrocytes contribute to MS progression.[36] To explore potential MS-specific astrocyte phenotypes, we reclustered astrocytes from iPSC-derived MS and HC cultures (Figures 3A, 3B, and S3A; Table S1). We identified eight distinct astrocyte subtypes, with cluster 6 almost exclusively consisting of MS-derived cells (Figures 3C, 3D, and S3B). Gene Ontology analysis of genes upregulated in this cluster showed enrichment for antigen processing and presentation, inflammatory signaling, and EBV infection (Figure 3E). Cluster 7, also enriched with MS-derived astrocytes (Figure S3C), was associated with inflammation-related genes including cytokine, interferon, and nuclear factor (NF)-κB signaling (Figure S3D). We also found that MS cultures were depleted of cells in cluster 3 (Figure S3E), which was linked to neuron development and sterol catabolism (Figure S3F). RNAscope *in situ* hybridization confirmed increased *HLA-DRA* expression in PPMS cultures, and immunofluorescence analysis showed a small increase at the protein level (Figures 3F–3J). These data suggest that, even in the absence of inflammatory stimuli, MS-derived astrocytes are more likely to acquire an inflammatory state at the expense of a neuro-supportive state, possibly contributing to disease progression.

Inflammatory reactive astrocytes undergo morphological changes that include a hypertrophic cell body with thicker processes[23,37] (Figure 3K). Therefore, we asked whether the presence of inflammatory clusters could lead to variations in morphological features that distinguish MS astrocytes. To assess astrocyte morphology, we used computational methods[38] for analysis of GFAP staining and nuclei (DAPI). By extracting measured features from individual cells, we calculated binary prediction scores for each MS type compared with HC using a logistic regression model. Despite the complex and highly variable nature of astrocyte morphology, the model demonstrated accuracy in distinguishing between MS and HC astrocytes. Interestingly, it suggested that astrocytes in RRMS exhibited the most distinct phenotypes (Figures 3L and 3M). We investigated the most influential features for the algorithm's decision-making process (Table S3) and grouped them into five categories: *shape*, *granularity*, *texture*, *concentric*, and *intensity* (Figure S3G; Table S3). The model identified 7 *shape* parameters as critical for distinguishing RRMS cells, while *intensity* of DAPI and GFAP and *concentric* measures were associated with all types of MS. Notably, we found

Please cite this article in press as: Clayton et al., Patient iPSC models reveal glia-intrinsic phenotypes in multiple sclerosis, Cell Stem Cell (2024), https://doi.org/10.1016/j.stem.2024.08.002

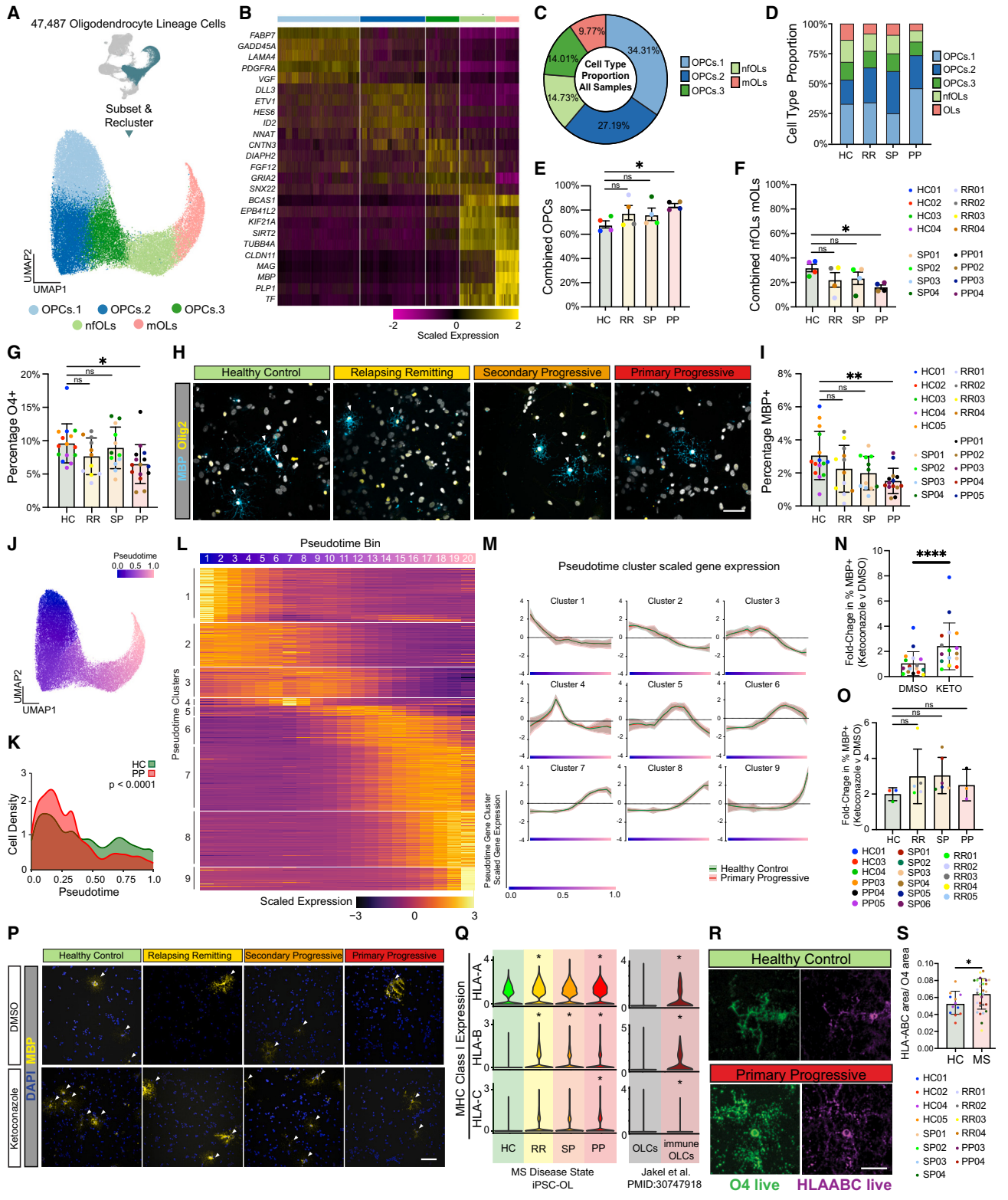

Figure 2. iPSC-derived cultures from people with MS contain fewer oligodendrocytes

(A) UMAP of 47,487 oligodendrocyte lineage cells subset and reclustered.

(B) Heatmap depicting the scaled expression of the top 5 enriched genes for each oligodendrocyte lineage cell cluster in (A).

(C) The proportion of each oligodendrocyte lineage cell type in iPSC-derived cultures from all samples.

(legend continued on next page)

Please cite this article in press as: Clayton et al., Patient iPSC models reveal glia-intrinsic phenotypes in multiple sclerosis, Cell Stem Cell (2024), https://doi.org/10.1016/j.stem.2024.08.002

pronounced differences in nuclear features, including multinucleated cells (Figures 3L and S3G), which align with the observation that reactive astrocytes frequently appear multinucleated and polyploid as a result of aberrant mitosis.[39] Thus, our morphological analysis supports the hypothesis that inflammatory clusters in MS astrocytes make them distinguishable from their healthy counterpart.

iPSC-derived MS astrocytes mirror pathological astrocytes in MS brains

Astrocytes can adopt an inflammatory pathological state in response to the microglial-derived cytokines tumor necrosis factor (TNF), interleukin (IL)-1α, and C1q (TIC)[23,37,40] and these TIC-induced neurotoxic reactive astrocytes have been observed in many neurodegenerative diseases, including MS.[37,41] Analysis of human iPSC-astrocytes has also shown that cells containing a common MS risk SNP express higher levels of genes associated with TIC-induced astrocyte reactivity.[42] We therefore sought to investigate whether, even in the absence of inflammatory stimuli, the iPSC-derived astrocytes in MS cultures reflect a similar pathological state. To do this, we integrated iPSC-astrocytes from HC and MS with single-cell analysis of HC human iPSC-astrocytes treated with TIC cytokines.[23,24] Unbiased clustering of this integrated dataset identified 12 distinct astrocyte clusters (Figure S4A; Table S4), three of which (clusters 8, 9, and 10) almost exclusively contained iPSC-derived astrocytes from all clinical MS subtypes and TIC-treated iPSC-derived astrocytes from healthy individuals (Figures S4B and S4C). Moreover, Gene Ontology analysis of genes defining these clusters showed enrichment for terms associated with inflammation and immune processes including antigen processing and presentation, cytokine signaling, and again EBV infection (Figures S4D–S4I). Together, these data show that iPSC-derived astrocytes from all clinical subtypes of MS transition to a pathological reactive state, independent of exogenous inflammatory stimuli or interaction with immune cells.

Finally, we sought to determine whether the iPSC-derived astrocyte subtype enriched in MS cultures corresponds to a pathological state found in the MS brain by integrating iPSC-derived astrocytes with available single-nucleus data from MS brain tissues.[12] We identified 7 distinct integrated astrocyte clusters (Figure 4A; Table S4). Two integrated clusters (4 and 5) contained almost exclusively cells from MS brains and iPSC-derived MS cultures (Figures 4B–4D and S4J). Cluster 5, which included cells from all MS subtypes, showed enrichment in MHC class I and class II genes and was associated with antigen processing and presentation, inflammatory signaling, neurodegeneration, and EBV infection (Figures 4E and 4F). Cluster 4, enriched with cells from a single MS brain and iPSC-astrocytes from a single donor, showed increased expression of heat shock response genes and was associated with cell stress response (Figures S4J–S4L). These data show that iPSC-derived CNS cultures from people with MS generate pathological astrocyte subtypes that mirror those in MS brains, even without inflammatory stimuli or peripheral immune activation.

(D) The proportion of each oligodendrocyte lineage cell type in iPSC-derived cultures from HC, RRMS, SPMS, and PPMS lines.
(E) Percentage of OPCs in iPSC-derived cultures from HC, RRMS, SPMS, and PPMS lines. The percentage of OPCs in PP cultures is higher than in HC cultures. Data presented as mean ± SEM for $n = 4$ per group. p value generated by Welch's ANOVA with Dunnett's T3 correction for multiple comparisons against HC. Data are complementary to (F).
(F) Percentage of newly formed oligodendrocytes (nfOLs) or mature oligodendrocytes (mOLs) in iPSC-derived cultures from HC, RRMS, SPMS, and PPMS lines. The percentage of combined nfOLs and mols in PP cultures is lower than in HC cultures. Data presented as mean ± SEM for $n = 4$ per group. p value generated by Welch's ANOVA with Dunnett's T3 correction for multiple comparisons against healthy controls (HCs). Data are complementary to (E).
(G) Percentage of $O4^+$ early oligodendrocytes in iPSC-derived cultures from HC, RRMS, SPMS, and PPMS lines. The percentage of $O4^+$ oligodendrocytes is lower in PP cultures than in HC cultures. Error bars show mean ± standard deviation ($n = 3$ wells per line for 4–5 lines per group). p values generated by one-way ANOVA with Dunnett's correction for multiple comparisons.
(H) Representative images of iPSC-derived glial cultures stained for OLIG2 (yellow) and for MBP (teal). Nuclei in gray (DAPI). Scale bars, 50 μm.
(I) Percentage of MBP^+ oligodendrocytes in iPSC-derived cultures from HC, RRMS, SPMS, and PPMS lines. The percentage of MBP^+ oligodendrocytes is lower in PP cultures than in HC cultures. Error bars show mean ± standard deviation ($n = 3$ wells per line for 4–5 lines per group). p values generated by one-way ANOVA with Dunnett's correction for multiple comparisons.
(J) Pseudotime plot of oligodendrocyte lineage trajectory from OPCs to mature oligodendrocytes.
(K) Cell density plot that shows the distribution of cells across the oligodendrocyte lineage trajectory from OPCs to mature oligodendrocytes for iPSC-derived cells from HC or PPMS. p value generated with a two-sample Kolmogorov-Smirnov test.
(L) Heatmap depicting the scaled expression of genes that were determined to have pseudotime-specific expression profiles. Pseudotime gene modules were determined using oligodendrocyte lineage cells from HC lines only.
(M) Comparison of pseudotime gene expression profiles between HC and PPMS oligodendrocyte lineage cells. Pseudotime gene modules were determined using oligodendrocyte lineage cells from HC lines only.
(N) Percentage of MBP^+ cells in all cultures treated with vehicle (DMSO) or ketoconazole. Error bars show mean ± standard deviation ($n = 17$ lines; each datapoint corresponds to the average of 2 technical replicates per line). p values generated by two-way paired t test.
(O) Fold-change in the percentage of MBP^+ cells in HC, RRMS, SPMS, and PPMS cultures treated with either vehicle (DMSO) or ketoconazole. Data are presented as mean ± standard deviation for $n = 3$–6 lines per group; each datapoint corresponds to the average of 2 technical replicates per line. p values generated by one-way ANOVA with Dunnett's correction for multiple comparisons.
(P) Representative images of HC, RRMS, SPMS, and PPMS cultures treated with either vehicle (DMSO) or ketoconazole. Scale bar, 100 μM.
(Q) Expression of MHC class I genes in HC, RRMS, SPMS, and PPMS cultures. Expression of MHC class I genes in oligodendrocyte lineage cells (OLCs) and immunological OLCs from MS postmortem brain (PMID: 30747918). p value generated by Wilcoxon ranked sum test within the Seurat R package. $^*p < 0.05$.
(R) Representative immunofluorescence images of oligodendrocytes from HC and PPMS cultures stained for the live markers O4 (green) and HLA-ABC (purple). Scale bar, 50 μm.
(S) Quantification of HLA-ABC area within O4 area shows that oligodendrocytes from MS cultures have increased HLA-ABC proteins on their surface. Error bars show mean ± standard deviation ($n = 4$ HC and 10 MS lines with 3 wells per line). Each datapoint represents the per-well average of 25 fields of view. p values generated by one-way unpaired t test.

Please cite this article in press as: Clayton et al., Patient iPSC models reveal glia-intrinsic phenotypes in multiple sclerosis, Cell Stem Cell (2024), https://doi.org/10.1016/j.stem.2024.08.002

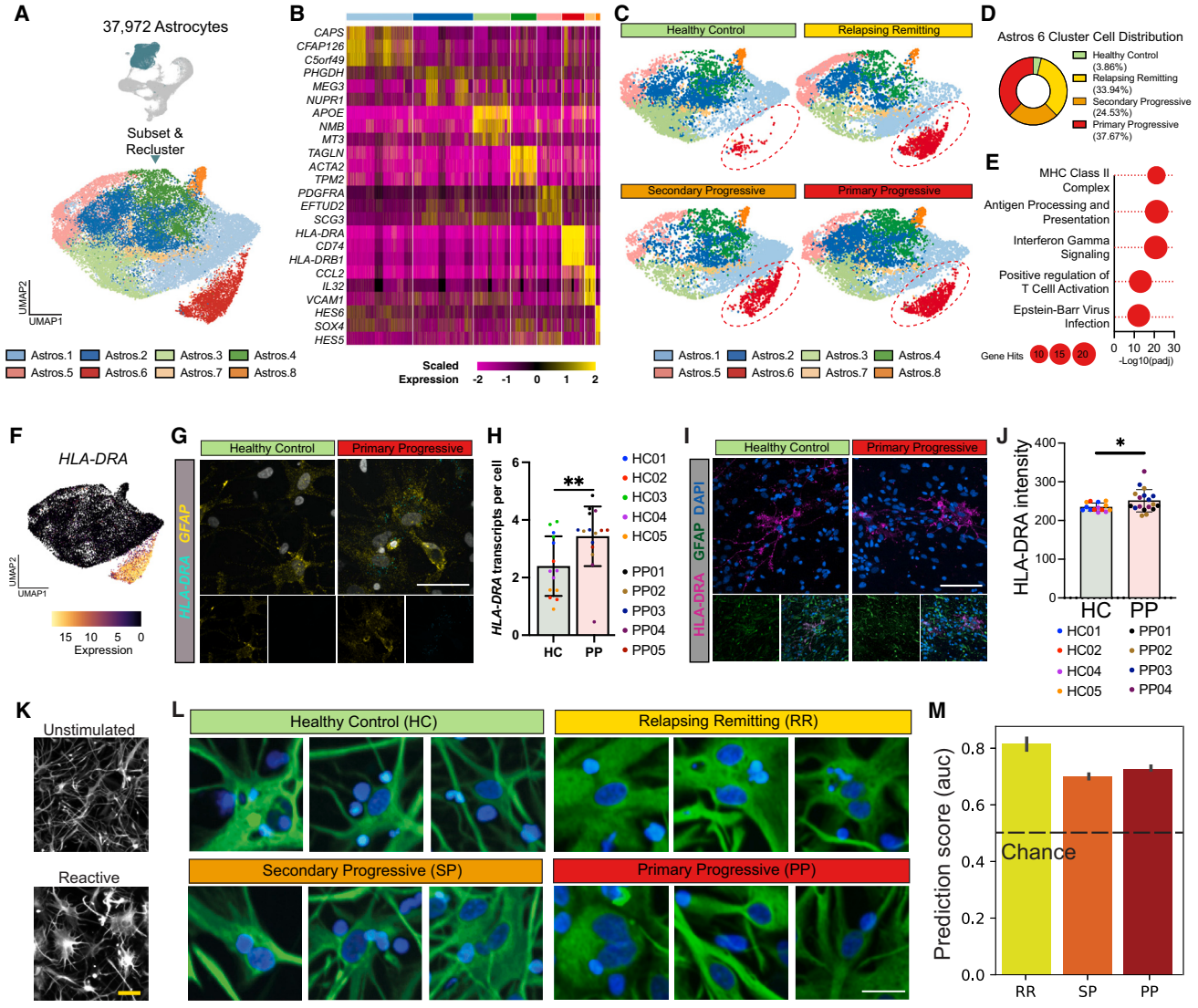

Figure 3. scRNA-seq reveals a reactive astrocyte subtype enriched in iPSC-derived MS cultures

(A) UMAP of 37,927 astrocytes subsetted and reclustered. Eight unique astrocyte subclusters were identified. Only cells identified as astrocytes in the initial clustering (Figure 1D light blue) were subsetted and used for reclustering.

(B) Heatmap showing the scaled expression of the top three genes enriched in each astrocyte subcluster.

(C) UMAP plots of HC, RRMS, SPMS, and PPMS iPSC-derived astrocytes. The Astro.6 cluster is enriched only in iPSC-derived astrocytes from MS and not HC.

(D) Distribution of HC, RRMS, SPMS, and PPMS iPSC-derived astrocytes in the astrocyte subcluster 6.

(E) Gene Ontology analysis of genes significantly increased in astrocyte subcluster 6 compared with all other astrocyte subclusters. *p* values were generated by gProfiler using the g:SCS algorithm.

(F) UMAP plot overlayed with the expression of *HLA-DRA*, a gene significantly increased in Astro.6 compared with all other astrocyte clusters.

(G) Representative images of RNAscope *in situ* hybridization for *GFAP* and *HLA-DRA* in iPSC-derived cultures from HC and PPMS. Images show localization of *HLA-DRA* to *GFAP*$^+$ astrocytes; Hoechst is in gray. Scale bars, 50 μm.

(H) Quantification of RNAscope *in situ* hybridization for *HLA-DRA* within *GFAP*$^+$ cells in iPSC-derived cultures from HC and PPMS. Error bars show mean ± standard deviation ($n = 5$ lines per group with 2–3 wells per line). Each datapoint represents the per-well average of 9 fields of view. *p* value generated by one-way unpaired t test.

(I) Representative images of healthy control (HC02) and primary progressive (PP04) cultures immunostained for GFAP (green) and HLA-DRA (magenta), with DAPI in blue. Scale bars, 100 μm.

(J) Quantification of HLA-DRA$^+$ immunostaining within the GFAP$^+$ population in iPSC-derived cultures from HC and PPMS lines showed increased protein levels in PPMS lines. Error bars show mean ± standard deviation ($n = 4$ lines per group with 3–5 wells per line). Each datapoint represents the per-well average of 9 fields of view. *p* value generated by one-way unpaired t test.

(K) Representative immunofluorescence images of unstimulated and TIC-reactive astrocytes to highlight the morphological changes. Cells are stained with GFAP; scale bars, 50 μm.

(legend continued on next page)

Please cite this article in press as: Clayton et al., Patient iPSC models reveal glia-intrinsic phenotypes in multiple sclerosis, Cell Stem Cell (2024), https://doi.org/10.1016/j.stem.2024.08.002

DISCUSSION

MS results from the interaction between environmental factors, like EBV infection, and genetic predisposition[3] associated with peripheral immune and glial cells.[2,14] The role of glial cell-intrinsic dysfunction in MS initiation and progression remains unclear.[43,44] Here, we leveraged iPSC technologies to address this issue by investigating human glial cells independent of the complex *in vivo* environment, which is chronically altered by inflammation and infiltration of peripheral immune cells.

A handful of studies investigated iPSC-derived neural progenitors and oligodendrocytes from people with MS but used a limited number of lines (up to 3) and produced conflicting results.[45–49] Leveraging an automated platform, we generated HC, RRMS, SPMS, and PPMS iPSC lines and differentiated them into glia-enriched cultures. Single-cell transcriptome analysis revealed intrinsic MS oligodendrocytes and astrocytes features, including fewer oligodendrocytes in PPMS cultures that may be due to increased ferroptosis rather than impaired differentiation. Evidence of ferroptosis is found in active and chronic lesions and in cerebral spinal fluid of MS patients.[50] Ferroptosis has also been reported to induce oligodendrocyte death in the MS cuprizone model[51] and in the demyelinating Pelizaeus-Merzbacher disease.[52] Studies not involving iPSC modeling suggest that deficits in myelin may act as an initial trigger for MS, leading to the release of antigens that activate and promote the infiltration of peripheral immune cells—a concept known as the "inside-out" hypothesis.[43] This contrasts with the autoimmune hypothesis ("outside-in"), which claims that autoimmune cells in the periphery initiate the disease by infiltrating and attacking myelinated neurons. Analysis of postmortem MS brains and a mouse model of oligodendrocyte ablation[53] support the inside-out hypothesis, suggesting structural myelin abnormalities as the initial trigger of inflammation and demyelination[54–56] implicating intrinsic oligodendrocyte degeneration. Recent epigenetic studies also showed oligodendrocytes play a critical role in MS initiation, being primed at the chromatin level to activate immune genes.[57] Increased immune and inflammatory gene expression in oligodendrocyte lineage cells and astrocytes observed *in vitro* mirrors the transition to an immune-like state observed in postmortem MS brains.[11,34,35] Nevertheless, the etiology of these cells and their effect on de/remyelination in MS remains unclear. Applying deep learning for high-content imaging enables population-scale morphological profiling of cellular phenotypes to identify disease signatures not detectable by the human eye alone.[58] Indeed, using computational methods, we identified disease signatures in astrocytes, particularly in RRMS, distinguishing MS cells from HC and highlighting features typical of reactive astrocytes. Given that glial cells in our cultures were never exposed to inflammation or peripheral immune cells, our findings indicate that oligodendrocyte lineage cells and astrocytes in MS are intrinsically primed to acquire an immune-like state. Identifying MS susceptibility genes and SNPs in oligodendrocytes and other glial cells may hold the key to understanding variability in disease severity and progression.[14] Therefore, human glial cells generated using reprogramming technologies (from iPSCs or transdifferentiated from fibroblasts to preserve epigenetic features) will be critical for exploring genetic variance and regulatory sequences that cannot be investigated using animal models.

In conclusion, our study demonstrates that iPSC-derived glial-enriched cultures from people with MS are a powerful model to identify CNS-intrinsic phenotypes in MS. Future studies using human iPSC-derived models are necessary to fully understand glial contributions to MS pathogenesis. These findings could unveil novel glia-specific therapeutic targets to halt or reverse MS progression.

Limitations of the study

While this study includes the largest cohort of iPSCs from people with MS reported to date, it remains too small to identify genotype-phenotype associations. Line-to-line variability is a known challenge in the iPSC modeling field that can only be addressed by increasing statistical power and validating these findings with additional lines from more individuals. A limitation of our model is its failure to achieve myelination, likely due to the sparse axonal density and immature nature of the neurons present under these culture conditions. As a result, arborized oligodendrocytes, unable to contact axons and initiate myelination, undergo cell death, similar to what occurs during development.[59,60] Thus, future investigations will require the development of robust myelinating platforms for human cells—currently not available—similar to those established with mouse oligodendrocytes,[61] to explore potential intrinsic deficits in oligodendrocytes leading to myelin abnormalities and demyelination. The differentiation protocol used also lacks microglia and generates spinal cord-patterned glia. Additional studies with iPSC-derived microglia, neurons, and other regional specifications are warranted.

STAR★METHODS

Detailed methods are provided in the online version of this paper and include the following:

- KEY RESOURCES TABLE
- RESOURCE AVAILABILITY
  - Lead contact
  - Materials availability
  - Data and code availability
- EXPERIMENTAL MODEL AND SUBJECT DETAILS
  - iPSC generation, quality control, and culture conditions
  - iPSC differentiation into glia-enriched cultures
  - iPSC differentiation into cortical neurons
  - Cell dissociation and library preparation for single-cell RNA sequencing (scRNAseq)
  - scRNAseq data processing
  - Identification of broad shared cell types across integrated scRNA-seq samples
  - scRNAseq analysis of oligodendrocytes

(L) Most representative cells from each MS type and controls. For each model, we ranked the cells by probability of belonging to the class. Here, the top-scoring ones are presented. Scale bar, 25 μM.

(M) Binary prediction area under the curve (AUC) of a logistic regression model trained on healthy versus each MS line individually in astrocytes. The error bar represents the standard deviation of the AUC between cross-validation folds. The analysis is performed at site-level averages, with 1 site per well held out for training.

Please cite this article in press as: Clayton et al., Patient iPSC models reveal glia-intrinsic phenotypes in multiple sclerosis, Cell Stem Cell (2024), https://doi.org/10.1016/j.stem.2024.08.002

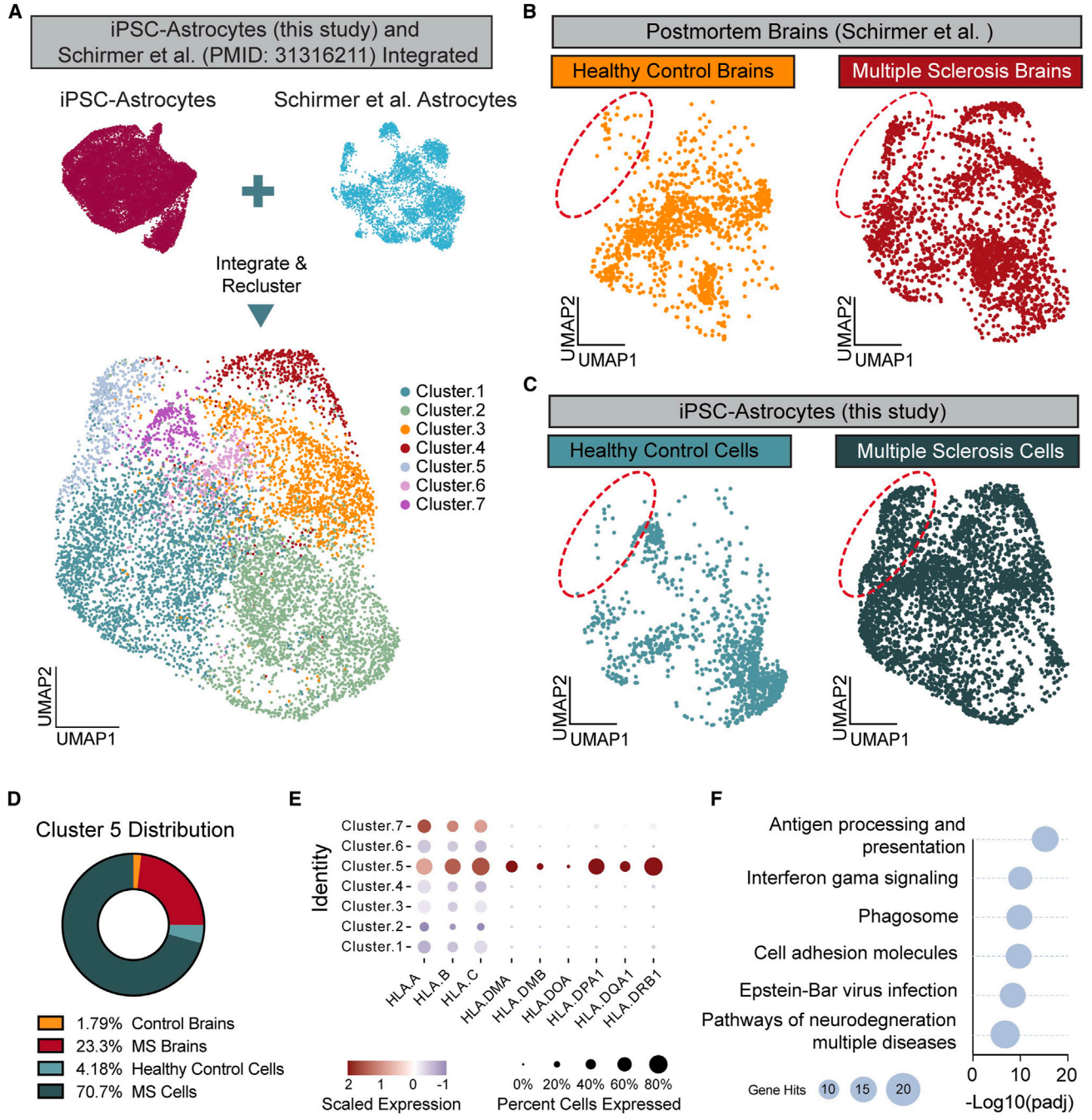

Figure 4. iPSC-derived astrocytes from people with MS mirror astrocytes from MS brains

(A) UMAP plot of iPSC-astrocytes integrated with astrocytes from postmortem brains (PMID: 31316211).

(B) UMAP plots showing the distribution of cells from healthy control brains and MS brains. Cluster 5 (red circle) is enriched for cells from MS brains.

(C) UMAP plots showing the distribution of cells from iPSC-derived astrocytes from HC and MS cultures. Cluster 5 (red circle) is enriched for iPSC-derived astrocytes from MS cultures.

(D) Distribution of cells from healthy control brains (yellow), MS brains (red), HC iPSC-derived astrocytes (light blue), and MS iPSC-derived astrocytes (dark blue) in cluster 5 of the integrated datasets.

(E) Dot plot showing the scaled expression of some MHC class I and class II genes in each of the clusters from the integrated datasets.

(F) Gene Ontology analysis of the top 100 genes enriched in cluster 5 of the integrated dataset compared with all other clusters in the integrated dataset. *p* values were generated by gProfiler uisng the Benjamini-Hochberg FDR approach.

SUPPLEMENTAL INFORMATION

Supplemental information can be found online at https://doi.org/10.1016/j.stem.2024.08.002.

ACKNOWLEDGMENTS

This study was supported by grants from the Department of Defense Congressionally Directed Medical Research Programs (CDMRP) Multiple Sclerosis Research Program (MSRP), award number DOD W81xWH-15-1-0448 (P.C.); the New York State Stem Cell Science (NYSTEM), award number C32586GG (V.F.); the National Multiple Sclerosis Society Career Transition Award TA-2105-37619 (B.L.L.C.); the National Institutes of Health, R35NS116842 (P.J.T.), R35NS111604 (P.C.), and sTF5 Care (P.J.T.); and by the New York Stem Cell Foundation Research Institute. We thank Dr. Raeka Aiyar for manuscript editing. We are extremely grateful to the Corinne Goldsmith Dickinson Center for Multiple Sclerosis and the people who donated the skin biopsies for this study. The graphical abstract and Figure 1A were created with Biorender.com.

AUTHOR CONTRIBUTIONS

Conceptualization, B.L.L.C., L.B., P.J.T., and V.F.; methodology, B.L.L.C. and L.B.; validation, B.L.L.C. and L.B.; formal analysis, B.L.L.C. and L.B.; investigation, B.L.L.C., L.B., M.S., T.R., B.M., K.K., D.M., D.P., K.B., and C.R.; resources, P.C., I.K.S., P.J.T., and V.F.; data curation, B.L.L.C.; writing – original draft, B.L.L.C., L.B., P.J.T., and V.F.; writing – review and editing, all co-authors; project administration, P.J.T. and V.F.; funding acquisition, P.J.T., P.C., and V.F.

DECLARATION OF INTERESTS

P.J.T. and B.L.L.C. are listed as inventors on issued and pending patent claims covering compositions and methods of enhancing glial cell function. P.J.T. is a co-founder and consultant for Convelo Therapeutics, which has licensed patents from Case Western Reserve University (CWRU). P.J.T. and CWRU retain equity in Convelo Therapeutics. V.F. and L.B. are listed as inventors on issued and pending patent claims covering glial cell generation methods.

Received: July 27, 2023
Revised: June 17, 2024
Accepted: August 5, 2024
Published: August 26, 2024

REFERENCES

1. Compston, A., and Coles, A. (2008). Multiple sclerosis. Lancet *372*, 1502–1517. https://doi.org/10.1016/S0140-6736(08)61620-7.
2. Bjornevik, K., Cortese, M., Healy, B.C., Kuhle, J., Mina, M.J., Leng, Y., Elledge, S.J., Niebuhr, D.W., Scher, A.I., Munger, K.L., et al. (2022). Longitudinal analysis reveals high prevalence of Epstein-Barr virus associated with multiple sclerosis. Science *375*, 296–301. https://doi.org/10.1126/science.abj8222.
3. Hedström, A.K., Alfredsson, L., and Olsson, T. (2016). Environmental factors and their interactions with risk genotypes in MS susceptibility. Curr. Opin. Neurol. *29*, 293–298. https://doi.org/10.1097/WCO.0000000000000329.
4. Thompson, A.J., Baranzini, S.E., Geurts, J., Hemmer, B., and Ciccarelli, O. (2018). Multiple sclerosis. Lancet *391*, 1622–1636. https://doi.org/10.1016/S0140-6736(18)30481-1.
5. Lublin, F.D., Reingold, S.C., Cohen, J.A., Cutter, G.R., Sørensen, P.S., Thompson, A.J., Wolinsky, J.S., Balcer, L.J., Banwell, B., Barkhof, F., et al. (2014). Defining the clinical course of multiple sclerosis: the 2013 revisions. Neurology *83*, 278–286. https://doi.org/10.1212/WNL.0000000000000560.
6. Lassmann, H., van Horssen, J., and Mahad, D. (2012). Progressive multiple sclerosis: pathology and pathogenesis. Nat. Rev. Neurol. *8*, 647–656. https://doi.org/10.1038/nrneurol.2012.168.
7. Katz Sand, I. (2015). Classification, diagnosis, and differential diagnosis of multiple sclerosis. Curr. Opin. Neurol. *28*, 193–205. https://doi.org/10.1097/WCO.0000000000000206.
8. McGinley, M.P., Goldschmidt, C.H., and Rae-Grant, A.D. (2021). Diagnosis and treatment of multiple sclerosis: a review. JAMA *325*, 765–779. https://doi.org/10.1001/jama.2020.26858.
9. Goldschmidt, C., and McGinley, M.P. (2021). Advances in the treatment of multiple sclerosis. Neurol. Clin. *39*, 21–33. https://doi.org/10.1016/j.ncl.2020.09.002.
10. Mey, G.M., Mahajan, K.R., and DeSilva, T.M. (2023). Neurodegeneration in multiple sclerosis. Wires Mech. Dis. *15*, e1583. https://doi.org/10.1002/wsbm.1583.
11. Jäkel, S., Agirre, E., Mendanha Falcão, A., van Bruggen, D., Lee, K.W., Knuesel, I., Malhotra, D., Ffrench-Constant, C., Williams, A., and Castelo-Branco, G. (2019). Altered human oligodendrocyte heterogeneity in multiple sclerosis. Nature *566*, 543–547. https://doi.org/10.1038/s41586-019-0903-2.
12. Schirmer, L., Velmeshev, D., Holmqvist, S., Kaufmann, M., Werneburg, S., Jung, D., Vistnes, S., Stockley, J.H., Young, A., Steindel, M., et al. (2019). Neuronal vulnerability and multilineage diversity in multiple sclerosis. Nature *573*, 75–82. https://doi.org/10.1038/s41586-019-1404-z.
13. Absinta, M., Maric, D., Gharagozloo, M., Garton, T., Smith, M.D., Jin, J., Fitzgerald, K.C., Song, A., Liu, P., Lin, J.-P., et al. (2021). A lymphocyte-microglia-astrocyte axis in chronic active multiple sclerosis. Nature *597*, 709–714. https://doi.org/10.1038/s41586-021-03892-7.
14. Factor, D.C., Barbeau, A.M., Allan, K.C., Hu, L.R., Madhavan, M., Hoang, A.T., Hazel, K.E.A., Hall, P.A., Nisraiyya, S., Najm, F.J., et al. (2020). Cell type-specific intralocus interactions reveal oligodendrocyte mechanisms in MS. Cell *181*, 382–395.e21. https://doi.org/10.1016/j.cell.2020.03.002.
15. International; Multiple; Sclerosis; Genetics Consortium, Harroud, A., Stridh, P., McCauley, J.L., Saarela, J., Van Den Bosch, A.M.R., Engelenburg, H.J., Beecham, A.H., Alfredsson, L., and Alikhani, K. (2023). Locus for severity implicates CNS resilience in progression of multiple sclerosis. Nature *619*, 323–331. https://doi.org/10.1038/s41586-023-06250-x.
16. Lagomarsino, V.N., Pearse, R.V., Liu, L., Hsieh, Y.-C., Fernandez, M.A., Vinton, E.A., Paull, D., Felsky, D., Tasaki, S., Gaiteri, C., et al. (2021). Stem cell-derived neurons reflect features of protein networks, neuropathology, and cognitive outcome of their aged human donors. Neuron *109*, 3402–3420.e9. https://doi.org/10.1016/j.neuron.2021.08.003.
17. Seah, C., Breen, M.S., Rusielewicz, T., Bader, H.N., Xu, C., Hunter, C.J., McCarthy, B., Deans, P.J.M., Chattopadhyay, M., Goldberg, J., et al. (2022). Modeling gene × environment interactions in PTSD using human neurons reveals diagnosis-specific glucocorticoid-induced gene expression. Nat. Neurosci. *25*, 1434–1445. https://doi.org/10.1038/s41593-022-01161-y.
18. Wentling, M., Lopez-Gomez, C., Park, H.-J., Amatruda, M., Ntranos, A., Aramini, J., Petracca, M., Rusielewicz, T., Chen, E., Tolstikov, V., et al. (2019). A metabolic perspective on CSF-mediated neurodegeneration in

multiple sclerosis. Brain *142*, 2756–2774. https://doi.org/10.1093/brain/awz201.

19. Paull, D., Sevilla, A., Zhou, H., Hahn, A.K., Kim, H., Napolitano, C., Tsankov, A., Shang, L., Krumholz, K., Jagadeesan, P., et al. (2015). Automated, high-throughput derivation, characterization and differentiation of induced pluripotent stem cells. Nat. Methods *12*, 885–892. https://doi.org/10.1038/nmeth.3507.
20. Douvaras, P., Wang, J., Zimmer, M., Hanchuk, S., O'Bara, M.A., Sadiq, S., Sim, F.J., Goldman, J., and Fossati, V. (2014). Efficient generation of myelinating oligodendrocytes from primary progressive multiple sclerosis patients by induced pluripotent stem cells. Stem Cell Rep. *3*, 250–259. https://doi.org/10.1016/j.stemcr.2014.06.012.
21. Douvaras, P., and Fossati, V. (2015). Generation and isolation of oligodendrocyte progenitor cells from human pluripotent stem cells. Nat. Protoc. *10*, 1143–1154. https://doi.org/10.1038/nprot.2015.075.
22. International; Multiple; Sclerosis; Genetics Consortium (2019). Multiple sclerosis genomic map implicates peripheral immune cells and microglia in susceptibility. Science *365*, eaav7188. https://doi.org/10.1126/science.aav7188.
23. Barbar, L., Jain, T., Zimmer, M., Kruglikov, I., Sadick, J.S., Wang, M., Kalpana, K., Rose, I.V.L., Burstein, S.R., Rusielewicz, T., et al. (2020). CD49f is a novel marker of functional and reactive human iPSC-derived astrocytes. Neuron *107*, 436–453.e12. https://doi.org/10.1016/j.neuron.2020.05.014.
24. Barbar, L., Rusielewicz, T., Zimmer, M., Kalpana, K., and Fossati, V. (2020). Isolation of human CD49f+ astrocytes and in vitro iPSC-based neurotoxicity assays. Star Protoc. *1*, 100172. https://doi.org/10.1016/j.xpro.2020.100172.
25. Fard, M.K., van der Meer, F., Sánchez, P., Cantuti-Castelvetri, L., Mandad, S., Jäkel, S., Fornasiero, E.F., Schmitt, S., Ehrlich, M., Starost, L., et al. (2017). BCAS1 expression defines a population of early myelinating oligodendrocytes in multiple sclerosis lesions. Sci. Transl. Med. *9*, eaam7816. https://doi.org/10.1126/scitranslmed.aam7816.
26. Emery, B., Agalliu, D., Cahoy, J.D., Watkins, T.A., Dugas, J.C., Mulinyawe, S.B., Ibrahim, A., Ligon, K.L., Rowitch, D.H., and Barres, B.A. (2009). Myelin gene regulatory factor is a critical transcriptional regulator required for CNS myelination. Cell *138*, 172–185. https://doi.org/10.1016/j.cell.2009.04.031.
27. Zhang, S., Wang, Y., Zhu, X., Song, L., Zhan, X., Ma, E., McDonough, J., Fu, H., Cambi, F., Grinspan, J., et al. (2021). The Wnt effector TCF7l2 promotes oligodendroglial differentiation by repressing autocrine BMP4-mediated signaling. J. Neurosci. *41*, 1650–1664. https://doi.org/10.1523/JNEUROSCI.2386-20.2021.
28. Lubetzki, C., Zalc, B., Williams, A., Stadelmann, C., and Stankoff, B. (2020). Remyelination in multiple sclerosis: from basic science to clinical translation. Lancet Neurol. *19*, 678–688. https://doi.org/10.1016/S1474-4422(20)30140-X.
29. Najm, F.J., Madhavan, M., Zaremba, A., Shick, E., Karl, R.T., Factor, D.C., Miller, T.E., Nevin, Z.S., Kantor, C., Sargent, A., et al. (2015). Drug-based modulation of endogenous stem cells promotes functional remyelination in vivo. Nature *522*, 216–220. https://doi.org/10.1038/nature14335.
30. Lariosa-Willingham, K.D., Rosler, E.S., Tung, J.S., Dugas, J.C., Collins, T.L., and Leonoudakis, D. (2016). A high throughput drug screening assay to identify compounds that promote oligodendrocyte differentiation using acutely dissociated and purified oligodendrocyte precursor cells. BMC Res. Notes *9*, 419. https://doi.org/10.1186/s13104-016-2220-2.
31. Mei, F., Fancy, S.P.J., Shen, Y.-A.A., Niu, J., Zhao, C., Presley, B., Miao, E., Lee, S., Mayoral, S.R., Redmond, S.A., et al. (2014). Micropillar arrays as a high-throughput screening platform for therapeutics in multiple sclerosis. Nat. Med. *20*, 954–960. https://doi.org/10.1038/nm.3618.
32. Deshmukh, V.A., Tardif, V., Lyssiotis, C.A., Green, C.C., Kerman, B., Kim, H.J., Padmanabhan, K., Swoboda, J.G., Ahmad, I., Kondo, T., et al. (2013). A regenerative approach to the treatment of multiple sclerosis. Nature *502*, 327–332. https://doi.org/10.1038/nature12647.
33. Hubler, Z., Allimuthu, D., Bederman, I., Elitt, M.S., Madhavan, M., Allan, K.C., Shick, H.E., Garrison, E., T Karl, M., Factor, D.C., et al. (2018). Accumulation of 8,9-unsaturated sterols drives oligodendrocyte formation and remyelination. Nature *560*, 372–376. https://doi.org/10.1038/s41586-018-0360-3.
34. Kirby, L., Jin, J., Cardona, J.G., Smith, M.D., Martin, K.A., Wang, J., Strasburger, H., Herbst, L., Alexis, M., Karnell, J., et al. (2019). Oligodendrocyte precursor cells present antigen and are cytotoxic targets in inflammatory demyelination. Nat. Commun. *10*, 3887. https://doi.org/10.1038/s41467-019-11638-3.
35. Falcão, A.M., van Bruggen, D., Marques, S., Meijer, M., Jäkel, S., Agirre, E., Samudyata, F., Floriddia, E.M., Vanichkina, D.P., ffrench-Constant, C., et al. (2018). Disease-specific oligodendrocyte lineage cells arise in multiple sclerosis. Nat. Med. *24*, 1837–1844. https://doi.org/10.1038/s41591-018-0236-y.
36. Ponath, G., Park, C., and Pitt, D. (2018). The role of astrocytes in multiple sclerosis. Front. Immunol. *9*, 217. https://doi.org/10.3389/fimmu.2018.00217.
37. Liddelow, S.A., and Barres, B.A. (2017). Reactive astrocytes: production, function, and therapeutic potential. Immunity *46*, 957–967. https://doi.org/10.1016/j.immuni.2017.06.006.
38. Migliori, B., Bose, N., and Paull, D. (2023). ScaleFEx^{SM}: a lightweight and scalable method to extract fixed features from single cells in high-content imaging screens. Preprint at bioRxiv. https://doi.org/10.1101/2023.07.06.547985.
39. Sosunov, A., Wu, X., McGovern, R., Mikell, C., McKhann, G.M., and Goldman, J.E. (2020). Abnormal mitosis in reactive astrocytes. Acta Neuropathol. Commun. *8*, 47. https://doi.org/10.1186/s40478-020-00919-4.
40. Clayton, B.L.L., Kristell, J.D., Allan, K.C., Karl, M., Garrison, E., Maeno-Hikichi, Y., Sturno, A.M., Shick, H.E., Miller, R.H., and Tesar, P.J. (2021). Chemical inhibition of pathological reactive astrocytes promotes neural protection. Preprint at bioRxiv. https://doi.org/10.1101/2021.11.03.467083.
41. Liddelow, S.A., Guttenplan, K.A., Clarke, L.E., Bennett, F.C., Bohlen, C.J., Schirmer, L., Bennett, M.L., Münch, A.E., Chung, W.-S., Peterson, T.C., et al. (2017). Neurotoxic reactive astrocytes are induced by activated microglia. Nature *541*, 481–487. https://doi.org/10.1038/nature21029.
42. Ponath, G., Lincoln, M.R., Levine-Ritterman, M., Park, C., Dahlawi, S., Mubarak, M., Sumida, T., Airas, L., Zhang, S., Isitan, C., et al. (2018). Enhanced astrocyte responses are driven by a genetic risk allele associated with multiple sclerosis. Nat. Commun. *9*, 5337. https://doi.org/10.1038/s41467-018-07785-8.
43. Stys, P.K., and Tsutsui, S. (2019). Recent advances in understanding multiple sclerosis. F1000Res. *8*. F1000 Faculty Rev-2100. https://doi.org/10.12688/f1000research.20906.1.
44. 't Hart, B.A., Luchicchi, A., Schenk, G.J., Stys, P.K., and Geurts, J.J.G. (2021). Mechanistic underpinning of an inside-out concept for autoimmunity in multiple sclerosis. Ann. Clin. Transl. Neurol. *8*, 1709–1719. https://doi.org/10.1002/acn3.51401.
45. Starost, L., Lindner, M., Herold, M., Xu, Y.K.T., Drexler, H.C.A., Heß, K., Ehrlich, M., Ottoboni, L., Ruffini, F., Stehling, M., et al. (2020). Extrinsic immune cell-derived, but not intrinsic oligodendroglial factors contribute to oligodendroglial differentiation block in multiple sclerosis. Acta Neuropathol. *140*, 715–736. https://doi.org/10.1007/s00401-020-02217-8.
46. Mozafari, S., Starost, L., Manot-Saillet, B., Garcia-Diaz, B., Xu, Y.K.T., Roussel, D., Levy, M.J.F., Ottoboni, L., Kim, K.-P., Schöler, H.R., et al. (2020). Multiple sclerosis iPS-derived oligodendroglia conserve their properties to functionally interact with axons and glia in vivo. Sci. Adv. *6*, eabc6983. https://doi.org/10.1126/sciadv.abc6983.
47. Daviaud, N., Chen, E., Edwards, T., and Sadiq, S.A. (2023). Cerebral organoids in primary progressive multiple sclerosis reveal stem cell and oligodendrocyte differentiation defect. Biol. Open *12*, bio059845. https://doi.org/10.1242/bio.059845.

48. Plastini, M.J., Desu, H.L., Ascona, M.C., Lang, A.L., Saporta, M.A., and Brambilla, R. (2022). Transcriptional abnormalities in induced pluripotent stem cell-derived oligodendrocytes of individuals with primary progressive multiple sclerosis. Front. Cell. Neurosci. *16*, 972144. https://doi.org/10.3389/fncel.2022.972144.

49. Nishihara, H., Perriot, S., Gastfriend, B.D., Steinfort, M., Cibien, C., Soldati, S., Matsuo, K., Guimbal, S., Mathias, A., Palecek, S.P., et al. (2022). Intrinsic blood–brain barrier dysfunction contributes to multiple sclerosis pathogenesis. Brain *145*, 4334–4348. https://doi.org/10.1093/brain/awac019.

50. Van San, E., Debruyne, A.C., Veeckmans, G., Tyurina, Y.Y., Tyurin, V.A., Zheng, H., Choi, S.M., Augustyns, K., van Loo, G., Michalke, B., et al. (2023). Ferroptosis contributes to multiple sclerosis and its pharmacological targeting suppresses experimental disease progression. Cell Death Differ. *30*, 2092–2103. https://doi.org/10.1038/s41418-023-01195-0.

51. Jhelum, P., Santos-Nogueira, E., Teo, W., Haumont, A., Lenoël, I., Stys, P.K., and David, S. (2020). Ferroptosis mediates cuprizone-induced loss of oligodendrocytes and demyelination. J. Neurosci. *40*, 9327–9341. https://doi.org/10.1523/JNEUROSCI.1749-20.2020.

52. Nobuta, H., Yang, N., Ng, Y.H., Marro, S.G., Sabeur, K., Chavali, M., Stockley, J.H., Killilea, D.W., Walter, P.B., Zhao, C., et al. (2019). Oligodendrocyte death in Pelizaeus-Merzbacher disease is rescued by iron chelation. Cell Stem Cell *25*, 531–541.e6. https://doi.org/10.1016/j.stem.2019.09.003.

53. Traka, M., Podojil, J.R., McCarthy, D.P., Miller, S.D., and Popko, B. (2016). Oligodendrocyte death results in immune-mediated CNS demyelination. Nat. Neurosci. *19*, 65–74. https://doi.org/10.1038/nn.4193.

54. Caprariello, A.V., Rogers, J.A., Morgan, M.L., Hoghooghi, V., Plemel, J.R., Koebel, A., Tsutsui, S., Dunn, J.F., Kotra, L.P., Ousman, S.S., et al. (2018). Biochemically altered myelin triggers autoimmune demyelination. Proc. Natl. Acad. Sci. USA *115*, 5528–5533. https://doi.org/10.1073/pnas.1721115115.

55. Weil, M.-T., Möbius, W., Winkler, A., Ruhwedel, T., Wrzos, C., Romanelli, E., Bennett, J.L., Enz, L., Goebels, N., Nave, K.-A., et al. (2016). Loss of myelin basic protein function triggers myelin breakdown in models of demyelinating diseases. Cell Rep. *16*, 314–322. https://doi.org/10.1016/j.celrep.2016.06.008.

56. Shaharabani, R., Ram-On, M., Avinery, R., Aharoni, R., Arnon, R., Talmon, Y., and Beck, R. (2016). Structural transition in myelin membrane as initiator of multiple sclerosis. J. Am. Chem. Soc. *138*, 12159–12165. https://doi.org/10.1021/jacs.6b04826.

57. Meijer, M., Agirre, E., Kabbe, M., Van Tuijn, C.A., Heskol, A., Zheng, C., Mendanha Falcão, A., Bartosovic, M., Kirby, L., Calini, D., et al. (2022). Epigenomic priming of immune genes implicates oligodendroglia in multiple sclerosis susceptibility. Neuron *110*, 1193–1210.e13. https://doi.org/10.1016/j.neuron.2021.12.034.

58. Schiff, L., Migliori, B., Chen, Y., Carter, D., Bonilla, C., Hall, J., Fan, M., Tam, E., Ahadi, S., Fischbacher, B., et al. (2022). Integrating deep learning and unbiased automated high-content screening to identify complex disease signatures in human fibroblasts. Nat. Commun. *13*, 1590. https://doi.org/10.1038/s41467-022-28423-4.

59. Takada, N., and Appel, B. (2010). Identification of genes expressed by zebrafish oligodendrocytes using a differential microarray screen. Dev. Dyn. *239*, 2041–2047. https://doi.org/10.1002/dvdy.22338.

60. Almeida, R.G., and Lyons, D.A. (2017). On myelinated axon plasticity and neuronal circuit formation and function. J. Neurosci. *37*, 10023–10034. https://doi.org/10.1523/JNEUROSCI.3185-16.2017.

61. Kerman, B.E., Kim, H.J., Padmanabhan, K., Mei, A., Georges, S., Joens, M.S., Fitzpatrick, J.A.J., Jappelli, R., Chandross, K.J., August, P., et al. (2015). *In vitro* myelin formation using embryonic stem cells. Development *142*, 2213–2225. https://doi.org/10.1242/dev.116517.

62. Hu, B.-Y., Du, Z.-W., Li, X.-J., Ayala, M., and Zhang, S.-C. (2009). Human oligodendrocytes from embryonic stem cells: conserved SHH signaling networks and divergent FGF effects. Development *136*, 1443–1452. https://doi.org/10.1242/dev.029447.

63. Labib, D., Wang, Z., Prakash, P., Zimmer, M., Smith, M.D., Frazel, P.W., Barbar, L., Sapar, M.L., Calabresi, P.A., Peng, J., et al. (2022). Proteomic alterations and novel markers of neurotoxic reactive astrocytes in human induced pluripotent stem cell models. Front. Mol. Neurosci. *15*, 870085. https://doi.org/10.3389/fnmol.2022.870085.

64. Qi, Y., Zhang, X.-J., Renier, N., Wu, Z., Atkin, T., Sun, Z., Ozair, M.Z., Tchieu, J., Zimmer, B., Fattahi, F., et al. (2017). Combined small-molecule inhibition accelerates the derivation of functional cortical neurons from human pluripotent stem cells. Nat. Biotechnol. *35*, 154–163. https://doi.org/10.1038/nbt.3777.

65. Butler, A., Hoffman, P., Smibert, P., Papalexi, E., and Satija, R. (2018). Integrating single-cell transcriptomic data across different conditions, technologies, and species. Nat. Biotechnol. *36*, 411–420. https://doi.org/10.1038/nbt.4096.

66. Stuart, T., Butler, A., Hoffman, P., Hafemeister, C., Papalexi, E., Mauck, W.M., Hao, Y., Stoeckius, M., Smibert, P., and Satija, R. (2019). Comprehensive integration of single-cell data. Cell *177*, 1888–1902.e21. https://doi.org/10.1016/j.cell.2019.05.031.

67. Cannoodt, R., Saelens, W., Sichien, D., Tavernier, S., Janssens, S., Guilliams, M., Lambrecht, B., Preter, K.D., and Saeys, Y. (2016). SCORPIUS Improves Trajectory Inference and Identifies Novel Modules in Dendritic Cell Development. Preprint at bioRxiv. https://doi.org/10.1101/079509.

68. Saelens, W., Cannoodt, R., Todorov, H., and Saeys, Y. (2019). A comparison of single-cell trajectory inference methods. Nat. Biotechnol. *37*, 547–554. https://doi.org/10.1038/s41587-019-0071-9.

69. Liberzon, A., Birger, C., Thorvaldsdóttir, H., Ghandi, M., Mesirov, J.P., and Tamayo, P. (2015). The Molecular Signatures Database (MSigDB) hallmark gene set collection. Cell Syst. *1*, 417–425. https://doi.org/10.1016/j.cels.2015.12.004.

70. Pico, A.R., Kelder, T., van Iersel, M.P., Hanspers, K., Conklin, B.R., and Evelo, C. (2008). WikiPathways: pathway editing for the people. PLoS Biol. *6*, e184. https://doi.org/10.1371/journal.pbio.0060184.

71. Kanehisa, M., and Goto, S. (2000). KEGG: kyoto encyclopedia of genes and genomes. Nucleic Acids Res. *28*, 27–30. https://doi.org/10.1093/nar/28.1.27.

72. Fabregat, A., Sidiropoulos, K., Viteri, G., Forner, O., Marin-Garcia, P., Arnau, V., D'Eustachio, P., Stein, L., and Hermjakob, H. (2017). Reactome pathway analysis: a high-performance in-memory approach. BMC Bioinformatics *18*, 142. https://doi.org/10.1186/s12859-017-1559-2.

73. Zhou, N., Yuan, X., Du, Q., Zhang, Z., Shi, X., Bao, J., Ning, Y., and Peng, L. (2023). FerrDb V2: update of the manually curated database of ferroptosis regulators and ferroptosis-disease associations. Nucleic Acids Res. *51*, D571–D582. https://doi.org/10.1093/nar/gkac935.

74. Ashburner, M., Ball, C.A., Blake, J.A., Botstein, D., Butler, H., Cherry, J.M., Davis, A.P., Dolinski, K., Dwight, S.S., Eppig, J.T., et al. (2000). Gene ontology: tool for the unification of biology. The Gene Ontology Consortium. Nat. Genet. *25*, 25–29. https://doi.org/10.1038/75556.

75. Hafemeister, C., and Satija, R. (2019). Normalization and variance stabilization of single-cell RNA-seq data using regularized negative binomial regression. Genome Biol. *20*, 296. https://doi.org/10.1186/s13059-019-1874-1.

76. Speir, M.L., Bhaduri, A., Markov, N.S., Moreno, P., Nowakowski, T.J., Papatheodorou, I., Pollen, A.A., Raney, B.J., Seninge, L., Kent, W.J., et al. (2021). UCSC Cell Browser: visualize your single-cell data. Bioinformatics *37*, 4578–4580. https://doi.org/10.1093/bioinformatics/btab503.

Please cite this article in press as: Clayton et al., Patient iPSC models reveal glia-intrinsic phenotypes in multiple sclerosis, Cell Stem Cell (2024), https://doi.org/10.1016/j.stem.2024.08.002

STAR★METHODS

KEY RESOURCES TABLE

REAGENT or RESOURCE	SOURCE	IDENTIFIER
Antibodies		
Donkey anti-rat Alexa Fluor 488	Invitrogen	A21208; RRID: AB_2535794
Donkey anti-rat Alexa Fluor 555	Invitrogen	A21434; RRID: AB_2535855
Donkey anti-goat Alexa Fluor 555	Invitrogen	A21432; RRID: AB_2535853
Donkey anti-rabbit Alexa Fluor 647	Invitrogen	A31573; RRID: AB_2536183
Goat anti-mouse Alexa Fluor 488 IgM	Invitrogen	A21042; RRID: AB_141357
Goat anti-rat Alexa Fluor 555	Invitrogen	A21434; RRID: AB_2535855
Goat anti-rabbit Alexa Fluor 647		A21244; RRID: AB_2535812
Goat SOX10	R&D Systems	AF2864; RRID: AB_442208
Monoclonal HLA-ABC	ThermoFisher	MA5-11723; RRID: AB_10985125
Mouse O4	Gift from Dr. James Goldman, Columbia University	N/A
Rabbit OLIG2	Millipore Sigma	AV31464; RRID: AB_1854793
Rat CD49f (PE-conjugated)	BD Biosciences	561894; RRID: AB_396079
Rat MBP	Abcam	Ab7349 RRID: AB_305869
Chemicals, peptides, and recombinant proteins		
Accutase	Thermo Fisher Scientific	A1110501
Ascorbic acid	Sigma-Aldrich	A4403
BDNF	R&D Systems	11166_BD
Biotin	Sigma-Aldrich	B4639
B27 supplement	Thermo Fisher Scientific	17504001
B27 supplement minus vit A	Thermo Fisher Scientific	12587-010
DAPT	Tocris	2634
dbcAMP	Sigma-Aldrich	D0627
DMEM/F12	Thermo Fisher Scientific	11320033
DMSO	Thermo Fisher Scientific	35050061
Donkey Serum	Jackson ImmuneResearch	017-000-121
DPBS	Thermo Fisher Scientific	10010023
GDNF	R&D Systems	212-GD
Goat serum	Jackson ImmuneResearch	AB_2336990
Glutamax	Thermo Fisher Scientific	35050-079
HEPES	Thermo Fisher Scientific	15630080
HGF	R&D Systems	294-HGN
HOECHST	Thermo Fisher Scientific	H3570
IGF-1	R&D Systems	291-G1
Insulin solution	Millipore Sigma	I9278-100ml
Ketoconazole	Sigma-Aldrich	UC280
laminin	Life technologies	23017-015
LDN193189	ReproCELL	04-0074
MEM non essential amino acids	Thermo Fisher Scientific	11140050
mTeSR1	StemCell Technologies	85850
mTesR1 without select factors	StemCell Technologies	05896
Neurobasal	Thermo Fisher Scientific	21103049
N2 supplement	Gibco	17502-048
NT3	R&D Systems	11346-N3
Papain	Worthington	LK003153

(*Continued on next page*)

Please cite this article in press as: Clayton et al., Patient iPSC models reveal glia-intrinsic phenotypes in multiple sclerosis, Cell Stem Cell (2024), https://doi.org/10.1016/j.stem.2024.08.002

Continued

REAGENT or RESOURCE	SOURCE	IDENTIFIER
PDGFaa	R&D Systems	221-AA
Penicillin Streptavidin	Thermo Fisher Scientific	150770063
PFA	Electron microscopy science	15710
PD0325901	Selleck Chemicals	S1036
Poly-ornithine	Sigma-Aldrich	P3655
Retinoic Acid	Sigma-Aldrich	R2625
Saponin	Sigma-Aldrich	47036-50G-F
SB431542	Selleck Chemicals	S1067
Smoothened agonist	EMD Millipore	566660
SU5402	Selleck Chemicals	S7667
Synth-a-freeze	Life Technologies	A1254201
Tasin-1	Drew Adams, Case Western Reserve University	N/A
T3	Sigma-Aldrich	T2877
2-Mercaptoethanol	Thermo Fisher Scientific	21985023
Triton X	Sigma-Aldrich	T8787
XAV939	Tocris	N/A
Y27632	Stemgent	04-0012
Critical commercial assays		
Chromium Single Cell Chip G	10X Genomics	PN-2000177
Chromium i7 Multiplex Kit	10X Genomics	PN-120262
Deposited data		
scRNAseq from 16 lines	https://www.ncbi.nlm.nih.gov/geo	GSE238221
Experimental models: Cell lines		
Human: iPSC HC01	NYSCF	050659-01-MR
Human: iPSC HC02	NYSCF	051121-01-MR
Human: iPSC HC03	NYSCF	050743-01-MR
Human: iPSC HC04	NYSCF	051104-01-MR
Human: iPSC HC05	NYSCF	051106-01-MR
Human: iPSC RR01	NYSCF	AK0007-01-MR
Human: iPSC RR02	NYSCF	AK0028-01-MR
Human: iPSC RR03	NYSCF	AK0024-01-MR
Human: iPSC RR04	NYSCF	AK0014-01-MR
Human: iPSC RR05	NYSCF	AK0013-01-MR
Human: iPSC RR06	NYSCF	AK0027-01-MR
Human: iPSC SP01	NYSCF	AK0015-01-MR
Human: iPSC SP02	NYSCF	AK0026-01-MR
Human: iPSC SP03	NYSCF	AK0008-01-MR
Human: iPSC SP04	NYSCF	AK0011-01-MR
Human: iPSC SP05	NYSCF	AK0005-01-MR
Human: iPSC SP06	NYSCF	AK0012-01-MR
Human: iPSC PP01	NYSCF	AK0001-01-MR
Human: iPSC PP02	NYSCF	AK0009-01-MR
Human: iPSC PP03	NYSCF	AK0004-01-MR
Human: iPSC PP04	NYSCF	AK0010-01-MR
Human: iPSC PP05	NYSCF	AK0003-01-MR
Software and algorithms		
Adobe Illustrator	Adobe	N/A
Cell Ranger	10X Genomics	v3.0.2

(*Continued on next page*)

Continued

REAGENT or RESOURCE	SOURCE	IDENTIFIER
Harmony	PerkinElmer	N/A
Fiji	GNU General Public License	N/A
Prism	GraphPad	N/A
R	GNU Project	N/A
Seurat	R package	v3.2 and v4.2
SCORPIUS		v1.0
ClustifyR	Bioconductor	V1.15
Other		
40μm Flowmi Cell Strainers	SP Bel-Art	H13680-0040
Phenoplate 96-well black	PerkinElmer	6055300
Culture plates 24 wells	Cellvis	P24-1.5H-N
Culture plates 6 well	Nunc	14-832-11

RESOURCE AVAILABILITY

Lead contact

Further information and requests for resources and reagents should be directed to and will be fulfilled by the lead contact, Valentina Fossati (vfossati@nyscf.org).

Materials availability

We have generated a collection of MS iPSC lines (listed in the key resources table) to enable investigation of molecular mechanisms of CNS dysfunction and potential glial targets for therapeutic intervention. NYSCF Research Institute iPSC lines may be made available on request through the NYSCF Research Institute repository (http://nyscf.org/repository), upon material transfer agreement.

Data and code availability

- All single-cell RNA-sequencing data generated in this study have been deposited at Gene Expression Omnibus (https://www.ncbi.nlm.nih.gov/geo/) and are publicly available as of the date of publication. Accession numbers are listed in the key resources table.
- This paper does not report original code. Data analysis was performed with publicly available packages by following available tutorials. Parameters used for specific analysis are provided in the STAR Methods section.
- Any additional information required to reanalyze the data reported in this paper is available from the lead contact upon request.

EXPERIMENTAL MODEL AND SUBJECT DETAILS

iPSC generation, quality control, and culture conditions

iPSC lines were derived by reprogramming fibroblasts from skin biopsies. Dr. Ilana Katz Sand at the Corinne Goldsmith Dickinson Center for MS at Mount Sinai recruited MS patients, and performed clinical characterization to distinguish RRMS, PPMS and SPMS forms (registered clinical trial NCT02549703). The original study also involved collection of cerebrospinal fluid,[18] and other MS-specific assignments and thus excluded healthy individuals. Control iPSC lines were chosen from the NYSCF Research Institute repository, selecting for age- and sex- matched individuals (registered clinical trial NCT04270604). All iPSC lines were reprogrammed via modified mRNA technology, using the NYSCF Global Stem Cell Array®, a fully automated reprogramming process that minimizes line-to-line variability.[19] iPSCs were expanded onto Matrigel-coated dishes in mTeSR1 medium (StemCell Technologies) and passaged using enzymatic digestion with Stempro Accutase (ThermoFisher) for 3-5 minutes and re-plated in mTeSR1 medium with the addition of 10μM ROCK Inhibitor (Stemgent) for the first 24 hours. A total of 22 iPSC lines were used in this study. For each line a certificate of analysis (CoA) is provided, which includes the results for the following tests: sterility check, mycoplasma testing, karyotyping, identity test, and pluripotency check. Table 1 summarizes the demographic information of the individuals that donated the skin biopsies. Additional clinical information and whole genome sequencing of the MS lines may be provided on request. Method details

iPSC differentiation into glia-enriched cultures

In this protocol neural progenitors are patterned with SAG (for SHH signaling) and retinoic acid to mimic the pMN domain, a specific area of the developing spinal cord where OLIG2$^+$ progenitors arise to ultimately form oligodendrocytes and motor neurons.[62] Cells were grown at 5% CO_2 in a 37C incubator. hiPSCs were induced along the neural lineage and differentiated using our previously

Please cite this article in press as: Clayton et al., Patient iPSC models reveal glia-intrinsic phenotypes in multiple sclerosis, Cell Stem Cell (2024), https://doi.org/10.1016/j.stem.2024.08.002

published protocol.[21] Briefly, hiPSCs were plated at 1-2 x 10^5 cells per well on matrigel-coated six-well plates in mTeSR1 medium with 10 μM ROCK inhibitor Y27632 (Stemgent). Starting the following day, cells were fed daily with mTeSR1 medium (StemCell Technologies). Once distinct colonies of ~200 μm in diameter were formed, differentiation was induced (day 0). Details for the differentiation protocol can be found in our previous publications[23,63] and a schematic with media composition is provided in Figure S1C. Patterning with SAG and retinoic acid induces $OLIG2^+$ progenitor cells, that assemble in neurospheres. Around d30 of differentiation, $OLIG2^+$ cells-enriched neurospheres were plated into polyOrnithine/laminin-coated dishes to allow cell attachment and migration. This protocol is different from traditional 2D differentiations, in that it maintains a 3D neurosphere from which progenitor cells continue to migrate over the course of the differentiation. Radial glial cells anchor the sphere to the well and progenitors migrate out, proliferate and then generate neurons, astrocytes and oligodendrocytes in this precise order. As time progresses, the total number of cells growing adherent to the plate increases; MBP^+ oligodendrocytes began to appear around day 50, and their number increases over time. Because the neurosphere continue to release progenitor cells, these cultures are asynchronous, meaning that at each time point they contain cells at various stages of glial development. At the end of the differentiation, between day 70 and day 85, cultures were dissociated using different protocols depending on downstream analyses. For exposure to myelinating compounds, RNAscope and immunofluorescence analyses, cells were incubated for ~25 minutes with Accutase (ThermoFisher) and passed through a 70μm strainer. The resulting single-cell suspension was re-plated or sorted for CD49f (BD Biosciences) to purify CD49f positive astrocytes and enrich oligodendrocyte lineage cells within the CD49f negative fraction. The FACS protocol has been described in details previously.[24] Single cell suspensions were re-plated onto PO/Lam coated plates and 24 hours after plating, medium was switched to "glial medium" (Figure S1C), and cells were fed with two-third media changes every other day. For scRNAseq analyses, cultures were dissociated using papain, as detailed below.

iPSC differentiation into cortical neurons

Our oligodendrocyte differentiation protocol generates less than 15% neurons, which remain mostly immature (*i.e.* they do not show any electrophysiological activity). Thus, to assess the differentiation potential of MS lines toward neurons we used a well-established protocol that we previously developed to produce cortical neurons[24] with the following modifications: Neurobasal was used instead of Brainphys after day 15, and PD0325901, SU5402, DAPT, and ROCK inhibitor were taken out of the media at day 25.

Briefly, hiPSCs were plated in a 12-well plate in mTeSR1 media with 10μM ROCK inhibitor Y2732. Starting the next day (d0), cells were fed daily with neural induction medium with SB431542 (20 μM; Stemgent), LDN193189 (100nM; Stemgent), XAV939 (1 μM; Tocris). Neural induction medium consisted of 1:1 DMEM/F12 (ThermoFisher) and Neurobasal (ThermoFisher) with 1x Glutamax (Thermo Scientific), 1x N2 supplement (Gibco), and 1x B27 supplement without Vitamin A (Gibco). On day 10, the medium was switched to neural induction medium with XAV939 (1μM), with continuing daily media changes. On day 15, cells were dissociated using Accutase and either frozen in Synth-a-freeze or plated in neuronal medium at 50k/well in a PO/Lam coated 96-well plate. Neuronal medium consists of Neurobasal (StemCell Technologies; 05790) with 1xB27 supplement (ThermoFisher; 17504001), and 10 μM ROCK inhibitor. On day 16, the medium was switched to neuronal medium with BDNF (40ng/mL; R&D Systems, 248-BDB), GDNF (40ng/mL; R&D Systems 212-GD), Laminin (1μg/mL), dbcAMP (250 μM), ascorbic acid (200 μM), PD0325901 (10 μM; Selleck Chemicals), SU5402 (10 μM; Selleck Chemicals), DAPT (10 μM), and ROCK inhibitor (10μM).[64] Cells were fed every other day. Starting on day 25, cells were fed every other day with neuronal medium with BDNF (40ng/mL), GDNF (40ng/mL), Laminin (1mg/mL), dbcAMP (250 μM), ascorbic acid (200 μM).

Cell dissociation and library preparation for single-cell RNA sequencing (scRNAseq)

Day 85 cultures from 16 lines were detached enzymatically in parallel using papain (Worthington) and were filtered through 40μm Flowmi Cell Strainers to obtain a single cell suspension. Single cells were processed using the 10X Single Cell 30 v3.1Rev B protocol. Briefly, we loaded the Chromium Single Cell Chip G (10X Genomics; PN-2000177) with 7,000 cells/sample and we performed library preparation as per the Chromium Single Cell 30 Library & Gel Bead Kit manufacturer's recommendations (10X Genomics; PN-120237 and PN1000121). We used the Chromium i7 Multiplex Kit (10X Genomics; PN-120262). Quality control was performed using the Qubit 4 Fluorometer (ThermoFisher; Q33227) and the Agilent 4200 TapeStation system. The resulting cDNA library was sequenced on a NovaSeq/HiSeq 2x150 bp, and 50,000 reads per cell were obtained.

scRNAseq data processing

Sequence data were first processed by 10x Cell Ranger v3.0.2 to align reads to the human transcriptome build GRCh38, remove empty droplets, and generate a feature-barcode matrix. Preprocessing was then performed with Seurat v3.2.[65] Following the standard pre-processing tutorial for the Seurat analysis package (https://satijalab.org/seurat/archive/v2.4/pbmc3k_tutorial.html). For each individual sample, genes expressed in fewer than 3 cells, cells with greater than 10,000 genes captured, and cells with fewer than 1250 genes captures and percent mitochondrial reads above 25% were removed.

Identification of broad shared cell types across integrated scRNAseq samples

In order to first identify broad cell types that were shared across all of the samples we performed integration of the data at the sample level. Integration was performed with Seruat v3.2[66] following the standard integration workflow (https://satijalab.org/seurat/archive/v3.2/integration). Each individual sample was log-normalized and 2000 variable features were identified using "NormalizeData" and "FindVariableFeatures" with the "vst" method. Integration anchors were then identified using "FindIntegrationAnchors" with default

Please cite this article in press as: Clayton et al., Patient iPSC models reveal glia-intrinsic phenotypes in multiple sclerosis, Cell Stem Cell (2024), https://doi.org/10.1016/j.stem.2024.08.002

settings afterwhich the individual samples were integrated using "IntegrateData" with default settings. The integrated dataset was then scaled using "ScaleData" while using difference in cell cycle score, RNA count, and percent mitochondrial reads as variable to regress. Principal component analysis was then ran using "RunPCA" with npcs = 50, followed by clustering using "FindNeighbors" dims = 1:25, and "FindClusters" with resolution = 0.2. Finally, "RunUMAP" was performed with dims = 1:25 to generate UMAP plots.

Differential gene expression between broad cell type clusters was performed in Seurat using "FindAllMarkers" with the Wilcoxon ranked sum test to identify differentially expressed genes between individual cell type clusters versus all other clusters combined. Genes were then ranked by Log2FC, from largest to smallest, and the top 100 genes for each cell type cluster were identified. To generate differentially expressed genes between paired groups, for example when comparing all Healthy Control cells vs all combined MS cells, "FindMarkers" with the Wilcoxon ranked sum test was used.

scRNAseq analysis of oligodendrocytes

Analysis of oligodendrocyte lineage cells was performed in Seurat v4.2. Oligodendrocyte lineage cells were subsetted from the full data. These cells were then reanalyzed without integration to identify differences between samples and disease conditions. Data was log-normalized using "NormalizeData" and the top 2000 variable features were identified using "FindVariableFeatures". The data set was then scaled using "ScaleData" while using difference in cell cycle score, RNA count, percent mitochondrial reads, and culture derivation batch as variable to regress. Principal component analysis was then ran using "RunPCA" with npcs = 50, followed by clustering using "FindNeighbors" dims = 1:11, and "FindClusters" with resolution = 0.4. Finally, "RunUMAP" was performed with dims = 1:11 to generate UMAP plots.

Differential gene expression between oligodendrocyte lineage cell clusters was performed in Seurat using "FindAllMarkers" with the Wilcoxon ranked sum test to identify differentially expressed genes between individual cell type clusters versus all other clusters combined. To generate differentially expressed genes between paired groups "FindMarkers" with the Wilcoxon ranked sum test was used.

scRNAseq pseudotime analysis

Pseudotime analysis was performed using the Bioconductor package SCORPIUS (https://github.com/rcannood/SCORPIUS)[67] which in comparison of multiple single-cell trajectory inference methods was identified as one a few methods that performed well under all conditions.[68] Seurat UMAP embeddings for the oligodendrocyte lineage cells was used to infer a trajectory by calling "infer_trajectory". Candidate pseudotime genes were then called by using the Random Forest algorithm to rank genes according to their ability to predict the inferred trajectory of cells. Cells were then separated into 20 pseudotime bins across the oligodendrocyte lineage and the average scaled expression of candidate pseudotime genes for cells in each bin was calculated using the Seurat command "AverageExpression" and the result plotted on a heatmap ordered by pseudotime to identify pseudotime expression modules. This was done for both healthy control cells and cells from people with primary progressive MS to identify any changes in the expression pattern of pseudotime genes.

Analysis of cell death gene module expression in oligodendrocyte lineage cells

Gene modules for cell death pathways were curated from the literature and gene ontology databases. For apoptosis genes were combined from Hallmark M5902,[69] WikiPathways WP254,[70] KEGG HSA04210,[71] and Reactome R-HSA-109581.[72] For ferroptosis genes were combined from WikiPathways WP4313[70] and the FerrDBv2 database.[73] For necroptosis genes were combined from Biological Processes GO:0070266 and GO:0097527[74] and Reactome R-HAS-5218859.[72] For pyroptosis genes were combined from Reactome R-HAS-5620971[72] and Biological Processes GO:0070269.[74] Then the 'AddModuleScore' command in Seurat v4.2 was used to determine the average expression levels of the cell death gene modules within each oligodendrocyte lineage cell cluster.

scRNAseq analysis of astrocytes

Analysis of astrocytes was performed in Seurat v3.2. Astrocytes were subsetted from the full data and analyzed with integration across culture derivation batches and using SCTransform normalization (https://satijalab.org/seurat/archive/v3.2/integration)[75] because exploratory analysis showed significant batch effects. Following SCTransform normalization data was integrated across batches by using "SelectIntegrationFeatures" to select 1000 integration features, integration anchors were found with "FindIntegrationAnchors" with k.anchor = 20, and finally "IntegrateData" was ran with normalization.method = "SCT". Principal component analysis was then performed on the integrated data using "RunPCA" and npcs = 50, followed by clustering using "FindNeighbors" dims = 1:19, and "FindClusters" with resolution = 0.2. Finally, "RunUMAP" was performed with dims = 1:19 to generate UMAP plots.

Differential gene expression analysis was performed in Seurat. First "PrepSCTFindMarkers" was ran to prepare the SCTransform normalized data set for differential gene expression analysis. Then "FindAllMarkers" with the Wilcoxon ranked sum test was used to identify genes that are significantly enriched in each cluster compared to the data set as a whole. To generate differentially expressed genes between paired groups "FindMarkers" with the Wilcoxon ranked sum test was used.

scRNAseq Integration of astrocytes with public data

Single-cell astrocyte data generated in this study were integrated with available single-cell raw read counts and metadata for single-cell RNA of iPSC-derived astrocytes from healthy controls exposed to TNF, IL1a, and C1q.[23] Integration was performed using SCTransform integration in Seurat (https://satijalab.org/seurat/archive/v3.2/integration). Briefly, both data sets were downsampled

Please cite this article in press as: Clayton et al., Patient iPSC models reveal glia-intrinsic phenotypes in multiple sclerosis, Cell Stem Cell (2024), https://doi.org/10.1016/j.stem.2024.08.002

to 1500 astrocytes per group to ensure differences in cell number between groups didn't affect integration. SCTransform normalization was then performed, after which data was integrated across batches by using "SelectIntegrationFeatures" to select 3000 integration features, integration anchors were found with "FindIntegrationAnchors" with k.anchor = 5, and finally "IntegrateData" was ran with normalization.method = "SCT". Principal component analysis was then performed on the integrated data using "RunPCA" and npcs = 50, followed by clustering using "FindNeighbors" dims = 1:25, and "FindClusters" with resolution = 0.5. Finally, "RunUMAP" was ran with dims = 1:25 to generate UMAP plots.

Single-cell astrocyte data generated in this study were also integrated with available single-cell data of astrocytes from post-mortem brain tissue from people with MS.[12] The raw read counts and metadata for single-cell RNAseq from post-mortem MS brain tissue was acquired from the UCSC cell browser.[76] Single-cell astrocyte data from this study were integrated with MS astrocytes using SCTransform integration in Seurat (https://satijalab.org/seurat/archive/v3.2/integration). Briefly, both data sets were downsampled to 1250 astrocytes per group to ensure differences in cell number between groups didn't affect integration. SCTransform normalization was then performed, after which data was integrated across batches by using "SelectIntegrationFeatures" to select 3000 integration features, integration anchors were found with "FindIntegrationAnchors" with k.anchor = 5, and finally "IntegrateData" was ran with normalization.method = "SCT". Principal component analysis was then performed on the integrated data using "RunPCA" and npcs = 50, followed by clustering using "FindNeighbors" dims = 1:25, and "FindClusters" with resolution = 0.2. Finally, "RunUMAP" was ran with dims = 1:25 to generate UMAP plots.

For both integrated data sets, differential gene expression analysis was performed in Seurat using "FindAllMarkers" with the Wilcoxon ranked sum test to identify differentially expressed genes between unbiased clusters.

Ketoconazole and TASIN-1 treatment

To quantify MBP^+ oligodendrocytes after exposure to promyelinating drugs, we digested the cultures at the end of the differentiation and sorted for CD49 negative cells (enriched of oligodendrocyte lineage cells). This process (enzymatic digestion and sorting) results in cell death, particularly for mature oligodendrocytes, but allows us to seed an equal number of cells (25K cells per well), which is more suitable for drug screening. Thus, the percentage of MBP^+ cells in this experiment cannot be directly compared with the percentage of MBP^+ cells showed in Figure 2I. Cells were seeded onto Poly-ornithine/laminin-coated 96-well Perkin Elmer "phenoplates" and cultured for additional 7 days in glia maturation media with either vehicle (DMSO, 0.1%V/V), Ketoconazole (1μM) or TASIN-1 (0.1uM, kindly provided by Drew Adams, Case Western Reserve University) with feeds every other day, a total of 3 treatments. On Day 8 post replating, cells were fixed for immunostaining. For the TASIN-1 experiment, we included SOX10 and OLIG2 in addition to MBP in the panel. For statistical analysis each well is considered a technical replicate (2-3 replicates minimum).

Timepoint culture

For GFAP, MBP, MAP2 panel in Figures 1C and S1B, a fraction of the single cell suspension obtained at the end of the differentiation for scRNAseq analysis was replated onto poly-ornithine/laminin-coated 96-well plates for immunostaining. For SOX10, MBP, OLIG2, O4 immunostaining and analysis, one sphere per well was plated around differentiation day 30 onto 48-well NUNC plate, 24-well Cellvis plate or 96-well-plate (Perkin Elmer Phenoplate), maintained in appropriate differentiation medium and then fixed at day 55, day 65 or day 75. Each well with one sphere was considered a technical replicate. In the time course experiment, we used 5 HC and 5 PP lines in the first differentiation and 4 HC and 4 PP lines in a second, independent differentiation (performed at different time and by different operators). Thus, each data point represents the average of 2-5 wells (technical replicates) per line (biological replicate), across two independent differentiations.

Immunostaining

Cultures were fixed in 2% PFA in PBS (adding 4% PFA solution to wells containing the same amount of medium) for 10 minutes, washed 3x in PBS, and stored at 4°C. Samples were incubated for one hour at room temperature in blocking solution consisting of PBS with 0.1% saponin (for MBP) or 0.1% Triton-X for all other markers and 5% normal donkey serum, then incubated with primary antibodies (see table) in blocking solution overnight at 4°C. The next day, samples were washed 3x in PBS, and then incubated in secondary antibodies and DNA dye (Alexa Fluor 488, 568, 647, and Hoechst or DAPI) at a dilution of 1:500 in blocking solution for 2 hours at room temperature. For HLA ABC live staining, we used an antibody that recognizes all three HLA class I molecules (A,B,C). All blocking and antibody solutions were prepared at 2X concentration. For blocking, 100 μL of media was removed from each well and 100 μL of fresh media containing 10% goat serum was added per well (final 5% goat serum). Cultures were incubated in blocking solution for 15 min at 37°C. For staining with primary antibody, 100 μL volume was removed from each well and replaced with 100 μL of HLA-ABC (final dilution 1:100) prepared in media containing 10% goat serum. Cells were incubated with primary antibody for 45 min at 37°C. Cells were subsequently washed twice with media by removing 100 μL from each well and replacing with 100 μL of fresh media. For secondary antibody incubation, 100 μL of media was removed per well and replaced with AlexaFluor 555 goat anti-mouse IgG2a (final dilution 1:500) diluted in media containing 10% goat serum. Cultures were incubated with secondary antibody for 15 min at 37°C and washed 3 times with PBS before imaging.

Image Acquisition and Analysis

All image acquisition (except for images in Figure 3I) was done with the Opera Phenix High Content Screening system (Perkin Elmer) in confocal mode. For the 96-well plates, we collected 25 fields, 4 Z-planes per well at 10X magnification. When NUNC plates were

Please cite this article in press as: Clayton et al., Patient iPSC models reveal glia-intrinsic phenotypes in multiple sclerosis, Cell Stem Cell (2024), https://doi.org/10.1016/j.stem.2024.08.002

used, we included a 3D printed part to make them compatible with the automated microscope; Cellvis plate needed no modification. For the larger format plates, we acquired 60(48-well) or 109(24-well) fields, 4 Z-planes per well at 10X magnification. All analyses were done using the Harmony software (Perkin Elmer). In summary, the analysis first traced intact nuclei based on the DNA stain fluorescence and then selected nuclei that were larger than 40-50μm^2 surface area and had intensity levels lower than the brightness of pyknotic nuclei. We scored the positive cells by identifying the cell type marker positive surrounding region around the nuclei and selected cells based on the mean fluorescence intensity in the surrounding ROI. When appropriate, we used nuclear SOX10 and OLIG2 labels to further filter oligodendrocyte lineage cells before identifying MBP positive oligodendrocytes. For live cells without a nuclear stain, we used the built-in "Find Cells" module in Harmony to identify cells based on an immunostaining signal such as O4/MBP or HLA-ABC/DR. Percentage was calculated at well level: Total positive cells/Total nuclei X 100 in well. Drug treated well replicates were averaged for the fold change ratio calculations. Plots were generated with Prism analysis software. HLA-DRA immunofluorescence images (Figure 3I) were acquired on a Zeiss confocal microscope.

RNAscope and oligodendrocyte size measurements

At day 82 of the glial differentiation protocol, cells were dissociated, and replated in 96-well plates as described. For measuring oligodendrocyte size, cells were fixed in 2%PFA and stained for MBP as described above. Images were acquired at 40X using the Opera Phenix High-Content Screening System (PerkinElmer). Harmony software was used to measure the area of MBP^+ signal around the nucleus. For RNAscope experiments, cells were fixed 2 days after plating following the protocol provided by ACDBio. In brief, cells were washed once in PBS then fixed in 10% Neutral Buffered Formalin for 30 minutes at room temperature. After 2x PBS washes, cells were dehydrated by incubation in 50% ethanol at room temperature for 5 minutes, followed by 70% ethanol at room temperature for 5 minutes, then 100% ethanol at room temperature for 5 minutes. 100% ethanol was then removed and replaced with fresh 70% ethanol at room temperature for 10 minutes. Cells were then stored at -20°C. For the RNAscope assay, cells were rehydrated by incubation in 70% ethanol (200μL/well) at room temperature for 2 minutes, followed by 50% ethanol (200μL/well) at room temperature for 2 minutes, followed by PBS at room temperature for 1 minute, then finally in PBS for 10 minutes (200μL/well). PBS was removed, plates were placed in the Humidity Control Tray provided by ACDbio, and 33uL freshly diluted Protease III (1:10 in PBS) was added in each well. Humidity Control Tray was closed and incubated for 10 minutes at room temperature. Cells were then washed in PBS for 2 minutes (200μL/well) and this was repeated twice for a total of three washes. Staining was then performed using the ACDbio "Tech Note for using RNAscope HiPlex Alternate Display Module", and imaging was performed using the Opera Phenix High-Content Screening System (PerkinElmer). To quantify the RNA within each cell, we used a custom-made Python script for this experiment. First, the script calculated the maximum value of the reference wells for removing the contribution from the background. Then, for each dye we computed the max projection from the stack, we subtracted the background value found above, flat field corrected each image and finally normalized them between 0 and 1. Once we had one single image for each dye, we located the cells based on the nuclei image (using an Otsu's threshold-based approach). Then we similarly located the positive portion of the images for the dyes that identified the cell type (GFAP, MBP and PLP1), and selected all the nuclei that were positive for any dye. Then looped over each of the selected cells for each of the RNA stains and inspected whether there were positive pixels within a specified region of interest. Since the size of each RNA was of about 20 pixels, we divided the number of positive pixels by 20 to get the number of total RNAs.

This analysis generated a csv with one row for each of the analyzed cells, and one column for the reported number of RNAs and positivity for each of the reference dyes.

Astrocyte morphology analysis

At the end of the differentiation cells were dissociated, replated onto 96-well-plates, allowed to recover 48 hours and then fixed with 2% PFA. Cultures were stained for GFAP, MBP and PLP-1 and GFAP astrocytes were selected for further analysis. The entire analysis of GFAP astrocyte morphology was performed in Python using a pipeline that we recently developed.[38]

Preprocessing

We first computed the max projection from the stack of images to flatten the plane into one image. We then normalized the values between 1 and 0 cutting the highest 0.1 percentile and lower 10 to remove noise and debris.

Feature calculation

To extract the features measurements, we first located the cells using a custom made MaskRCNN algorithm and crop each cell into bounding boxes of fixed size (102 pixels per side). For each segmented cell we used a threshold-based algorithm to identify which cells were $GFAP^+$ astrocytes. Then we created a mask over the stained portion of the cell and used $ScaleFEx^{SM}$[38] (algorithm publicly available) to extract the features from the DNA channel and the channel correspondent to the positive cell type (GFAP). Briefly, *Shape* measurements were calculated over the mask of each segmented object and assessed spatial relationships of the object (*eg*. perimeter, area, compactness, etc.). *Granularity* was measured by convolving morphological operators of increasing size to assess the presence of repeating patterns; *Texture* is the probability of high or low value pixels in different directions and lengths. *Intensity* encompasses measurements of pixel values. *Concentric* measurements compute intensity and granularity measurements over concentric regions of increasing size. This entire computation resulted in a data frame containing all the measurements and the information about location and cell lines (n of total features is 1056). Each row contains the measurements of a unique cell.

Please cite this article in press as: Clayton et al., Patient iPSC models reveal glia-intrinsic phenotypes in multiple sclerosis, Cell Stem Cell (2024), https://doi.org/10.1016/j.stem.2024.08.002

Feature vector analysis

We first normalized each feature of the entire dataset between 0 and 1. We then assessed which cell type had the highest MS signal by training and testing a Logistic Regression (sklearn package) on cross validation folds of site averages. The folds consisted of 3 groups of 3 held out sites per well for testing, and 6 for training. Astrocytes resulted in the highest signal and was the cell type on which we performed the rest of the analysis. We then fitted the entire dataset using a logistic regression model (sklearn package) and a binary task of healthy *vs* each MS type. We removed the highly correlated features (Pearson's coefficient > 0.9) and ranked the uncorrelated features by importance for the decision process of the algorithm (model.coeff_). We then selected the 30 best performing features (number chosen by locating the sharp drop of the feature's coefficient) and grouped them into their major class to assess redundancy of a specific subtype of feature. We also stored these features and the relative coefficients in the provided Table S3. Finally, we plotted the cells with high confidence (the ones in Figure 3L have a predictive score above 0.98 for MS and below 0.02 for the healthy controls) to visually assess and interpret the very subtle phenotype expressed in cultured cells.

QUANTIFICATION AND STATISTICAL ANALYSIS

Statistics

For quantification of MBP^+ oligodendrocytes, 3 independent experiments (using different batches of reagents and by distinct operators) were performed, using a minimum of 16 iPSC lines. For OLIG2 and SOX10 quantification, two independent experiments were performed. All other experiments were performed one time with minimum 16 lines (except for TASIN-1 experiment, that was performed on 10 iPSC lines) and several wells per line as technical replicates.

The Graphpad Prism software was used for all statistical analyses. The statistical test used, n, and meaning of each datapoint is described in the figure legends. The definition of center and dispersion measures is also indicated in the figure legends. Outliers identified using the ROUT method were excluded. Statistical significance was considered as $p<0.05$ (*=p<.05; **=p<.01; ***=p<.001; ****=p<.0001).